

# Self-similar vortex clusters in the turbulent logarithmic region

By JUAN C. DEL ÁLAMO<sup>1</sup>, JAVIER JIMÉNEZ<sup>1,2</sup>  
PAULO ZANDONADE<sup>3</sup> AND ROBERT D. MOSER<sup>3†</sup>

<sup>1</sup>School of Aeronautics, Universidad Politécnica de Madrid, 28040 Madrid, Spain

<sup>2</sup>Center for Turbulence Research, Stanford University, Stanford, CA 94305, USA

<sup>3</sup>Department of Theoretical and Applied Mechanics, University of Illinois, Urbana, IL 61801, USA

(Received 15 April 2005 and in revised form 23 January 2006)

The organization of vortex clusters above the buffer layer of turbulent channels is analysed using direct numerical simulations at friction Reynolds numbers up to  $Re_\tau = 1900$ . Especial attention is paid to a family of clusters that reach from the logarithmic layer to the near-wall region below  $y^+ = 20$ . These tall attached clusters are markers of structures of the turbulent fluctuating velocity that are more intense than their background. Their lengths and widths are proportional to their heights  $\Delta_y$  and grow self-similarly with time after originating at different wall-normal positions in the logarithmic layer. Their influence on the outer region is measured by the variation of their volume density with  $\Delta_y$ . That influence depends on the vortex identification threshold, and becomes independent of the Reynolds number if the threshold is low enough. The clusters are parts of larger structures of the streamwise velocity fluctuations whose average geometry is consistent with a cone tangent to the wall along the streamwise axis. They form groups of a few members within each cone, with the larger individuals in front of the smaller ones. This behaviour is explained considering that the streamwise velocity cones are ‘wakes’ left behind by the clusters, while the clusters themselves are triggered by the wakes left by yet larger clusters in front of them. The whole process repeats self-similarly in a disorganized version of the vortex-streak regeneration cycle of the buffer layer, in which the clusters and the wakes spread linearly under the effect of the background turbulence. These results characterize for the first time the structural organization of the self-similar range of the turbulent logarithmic region.

---

## 1. Introduction

According to the classical theory (Townsend 1976, chap. 5), turbulent wall flows in the overlap layer are characterized by a constant flux of kinetic energy from small scales near the wall to large ones far from it. The intensity of the active wall-normal motions in that region scales with the friction velocity, and the impermeability of the wall limits their sizes to scales of the order of the wall distance  $y$ , which leads to a logarithmic dependence of the mean profile with  $y$ . That limitation does not apply to wall-parallel inactive motions, which can reach sizes much larger than  $y$ . The validity of these ideas has lately become increasingly clear, as we will see below, but they

† Present address: Mechanical Engineering Department, University of Texas at Austin, TX 78712-0292, USA.

are based on general physical considerations, and little is known about the coherent structures that take part in the dynamics of the overlap region.

Vortices are a particularly interesting kind of coherent structure, because their dynamics and their induced velocity fields can be analysed easily under certain assumptions. Most of the theoretical work about the role of vortical structures on the physics of the logarithmic layer is based on the work of Perry & Chong (1982), which has its roots in Townsend's (1976, §5.7) attached eddy model. These authors conceived turbulent wall flows as forests of self-similar wall-attached vortex loops, similar to Theodorsen's (1952) horseshoes, randomly distributed in space. In this model, the vortex forest contains all the vorticity in the flow and is responsible for the mean profile and for the velocity fluctuations. Later refinements of the model also consider the effect of detached small-scale vortices, of attached vortices with configurations different from a vortex loop, and of inhomogeneities in their spatial distribution (Perry, Henbest & Chong 1986; Perry & Marusic 1995; Marusic 2001).

While there is a considerable amount of laboratory and numerical data on the near-wall vortical structures (Robinson 1991*a*), there is much less information in the case of the logarithmic layer ( $100\nu/u_\tau \lesssim y \lesssim 0.1h$ , where  $\nu$  is the kinematic viscosity of fluid,  $u_\tau$  the friction velocity and  $h$  the flow thickness). This is due in part to the joint requirements of Reynolds numbers high enough to observe an overlap region, and of resolutions fine enough to represent the vortices. Another reason is the difficulty of employing systematic procedures in the analysis of vortices, well-defined mathematically and free from visualization artefacts.

Head & Bandyopadhyay (1981) performed smoke visualizations of boundary layers at Reynolds numbers based on the momentum thickness up to  $Re_\theta = 10\,000$ . They proposed that the boundary layer is composed of vortex loops inclined at  $45^\circ$  to the wall, sometimes arranged to form larger structures inclined at smaller angles to the surface, and extending across the layer. Their main conclusions were confirmed by the particle image velocimetry (PIV) experiments performed by Adrian, Meinhart & Tomkins (2000) and by Tomkins & Adrian (2003) in boundary layers up to  $Re_\theta = 7705$ , and by Christensen & Adrian (2001) in channels at friction Reynolds numbers up to  $Re_\tau = 1734$ . Adrian *et al.* (2000) put forward a model based on packets of hairpin vortices, aligned in the streamwise direction, which evolve from initial disturbances in the near-wall region. They suggested that the packets conserve their coherence as they age because all their members move at the same speed, and that the induced flow of each packet comes from the cooperative effect of several hairpins. Adrian *et al.* (2000) pointed out that different packets may also align in front of each other, inducing larger zones of low streamwise velocity, which they observed. These structures look like ramps aligned with the stream and inclined at an average angle of  $12^\circ$  to the wall. Christensen & Adrian (2001) gave statistical evidence of the existence of ramps, and of their association with trains of spanwise vortices inclined at  $13^\circ$ – $14^\circ$  to the wall. Tomkins & Adrian (2003) documented the model in wall-parallel planes, and proposed a mechanism of scale growth in the spanwise direction based on mergings of vortex packets. Ganapathisubramani, Longmire & Marusic (2003) carried out a similar study based on stereo PIV in a boundary layer at  $Re_\theta = 2500$ . They showed that structures with signatures of hairpin packets contain an important fraction of the Reynolds shear stresses, that they can reach lengths of around twice the thickness of the layer, and that their streamwise coherence breaks down beyond the logarithmic region.

The evidence from these laboratory experiments offers a simple connection between the hairpin packet paradigm and the classical theory. However, the observations are

constrained to two dimensions, and use fields of view which are too short to observe the large-scale organization of the overlap region. In addition, recent results suggest that it could be too soon to abandon other, less organized, interpretations. Del Álamo *et al.* (2004) found that in the logarithmic regions of turbulent channels up to  $Re_\tau = 1900$ , the spectral widths of the largest scales of the streamwise velocity are proportional to the square root of their lengths. Jiménez, Flores & García-Villalba (2001) suggested that this behaviour can be explained assuming that the associated structures are the wakes left by compact structures of the wall-normal velocity, which spread under the action of the incoherent background turbulence. Del Álamo *et al.* (2004) showed that streamwise laboratory spectra in pipes (Perry *et al.* 1986) and in boundary layers (Hites 1997) at higher Reynolds numbers are also consistent with this idea. Jiménez *et al.* (2004) used a similar model to explain the behaviour of the streamwise-velocity spectrum in the near-wall region.

The objective of this paper is to study the organization of clusters of intense vortices in turbulent channels, especially above the buffer layer, and to examine their relation with the structures of the velocity field. For this purpose we will use data from the numerical experiments of del Álamo & Jiménez (2003) and of del Álamo *et al.* (2004), whose Reynolds numbers,  $180 < Re_\tau < 1900$ , are comparable to those of most related laboratory experiments. Their numerical resolution is high enough to represent accurately small-scale regions of intense vorticity, and their computational boxes are large enough to capture the largest scales in the logarithmic and outer regions. An especial effort has been made to analyse the data in a well-defined systematic manner, and to offer statistical evidence as free as possible from subjective interpretations.

The present results indicate that the population of vortices in the logarithmic region breaks naturally into a wall-attached and a wall-detached family, similar to those in Perry *et al.* (1986). We will show that the former are actually indicators of the compact wall-normal motions that Jiménez *et al.* (2001) postulated to force large-scale streamwise velocity fluctuations, and that their sizes are similar to those of the structures with signatures of hairpin packets identified by Ganapathisubramani *et al.* (2003) and by Tomkins & Adrian (2003) at similar Reynolds numbers. We will present evidence that these tall attached clusters are self-similar, with lengths and widths proportional to their heights, and that they grow self-similarly with time from different wall-normal positions within the logarithmic layer. We will show that the influence of the tall attached clusters on the outer region depends on the vortex identification threshold, but that it is possible to choose a threshold for which that influence is roughly independent of the wall distance and of the Reynolds number.

We will see that the average velocity field conditioned to the presence of tall attached clusters reveals conical structures of streamwise velocity fluctuations, much larger than the conditioning objects. We will show that the clusters are arranged inside each cone in ascending order of size, consistent with the streamwise velocity structures being ‘wakes’ left behind the clusters, and with the clusters themselves being triggered by the upstream wakes left by yet larger clusters in front of them. The spreading of the conditional wakes will be explained to result from the competing linear effects of the advection by the mean profile and of the dispersion by the background turbulence, as suggested by Jiménez, del Álamo & Flores (2004) and by del Álamo *et al.* (2004). This model is described in more detail in del Álamo & Jiménez (2006) and del Álamo *et al.* (2006).

The paper is organized as follows. The numerical database is briefly described in §2, with emphasis on its spatial resolution. In §3, we explain the procedure employed

Case	Line	$Re_\tau$	$L_x/h$	$L_z/h$	$\Delta x^+$	$\Delta z^+$	$N_y$	$N_F$	$N_C$
L180	— · —	185	$12\pi$	$4\pi$	14	6.8	97	106	$3.8 \times 10^5$
L550	· · · · ·	547	$8\pi$	$4\pi$	13	6.7	257	23	$9.4 \times 10^5$
L950	— — —	934	$8\pi$	$3\pi$	11	5.7	385	18	$2.4 \times 10^6$
S950	○	964	$\pi$	$\pi/2$	12	5.8	385	111	$3.1 \times 10^5$
S1900	— — —	1901	$\pi$	$\pi/2$	12	5.8	769	63	$9.8 \times 10^5$

TABLE 1. Parameters of the experiments.  $L_x$  and  $L_z$  are the streamwise and spanwise dimensions of the numerical box and  $h$  is the channel half-width.  $\Delta x$  and  $\Delta z$  are the resolutions after dealiasing.  $N_y$  is the number of Chebychev polynomials.  $N_F$  is the number of fields used to accumulate statistics and  $N_C$  is the number of clusters extracted for the reference value of the identification threshold.

to identify vortices and to classify their clusters. The properties of the clusters, and their relation to the large-scale organization of the velocity field in the logarithmic region, are presented in §4. Finally, conclusions are given in §5.

## 2. The numerical experiments

We use data from the channel-flow simulations of del Álamo & Jiménez (2003) and of del Álamo *et al.* (2004). The numerical code integrates the Navier–Stokes equations in the form of evolution problems for the wall-normal vorticity  $\omega_y$  and for the Laplacian of the wall-normal velocity  $\nabla^2 v$ , as in Kim, Moin & Moser (1987). The spatial discretization uses dealiased Fourier expansions in the wall-parallel planes, and Chebychev polynomials in  $y$ . The streamwise and spanwise coordinates and velocity components are, respectively,  $x$ ,  $z$  and  $u$ ,  $w$ . The parameters of the simulations are summarized in table 1.

The characteristics of the present experiments with respect to the large scales of the outer region were documented in previous works (del Álamo & Jiménez 2003; del Álamo *et al.* 2004). Here we pay more attention to their spatial resolution, which is crucial to represent the vortices accurately. It is intermediate between those used by Moser, Kim & Mansour (1999) for their cases at  $Re_\tau = 180$  and  $Re_\tau = 590$ , and compares favourably with those used in most related numerical and laboratory studies (Blackburn, Mansour & Cantwell 1996; Adrian *et al.* 2000; Ganapathisubramani *et al.* 2003; Tanahashi *et al.* 2003, 2004).

In our simulations, the most under-resolved vorticity component is the spanwise vorticity in the streamwise direction. Figure 1 displays the longitudinal enstrophy spectral densities of this vorticity component,  $\phi_{\omega_z}(\lambda_x, y) = k_x \int \widehat{\omega}_z \widehat{\omega}_z^* dk_z$ , from the present experiments, where  $\widehat{\omega}_z$  is the Fourier coefficient of  $\omega_z$ , and  $k = 2\pi/\lambda$  is the wavenumber corresponding to a wavelength  $\lambda$ . The overbar will be used in this paper for averaging over the relevant homogeneous directions, in this case over time. The insufficient resolution of the smallest scales of  $\omega_z$  produces spurious accumulations of enstrophy in the short-wavelength tails of  $\phi_{\omega_z}$ , which is revealed by the ‘hooks’ of the curves in figures 1(a) and 1(b). Other enstrophy spectral densities show that the most under-resolved vorticity component in the spanwise direction is  $\omega_y$ . The under-resolved enstrophies contained in the ‘hooks’, defined as the integrals of the spectra from their smallest wavelength to the location of their minima, are less than 3.1 % of  $\overline{\omega_z^2}$  in  $x$  and 2.3 % of  $\overline{\omega_y^2}$  in  $z$ , at all wall distances and for all the simulations. Figure 1(b) shows

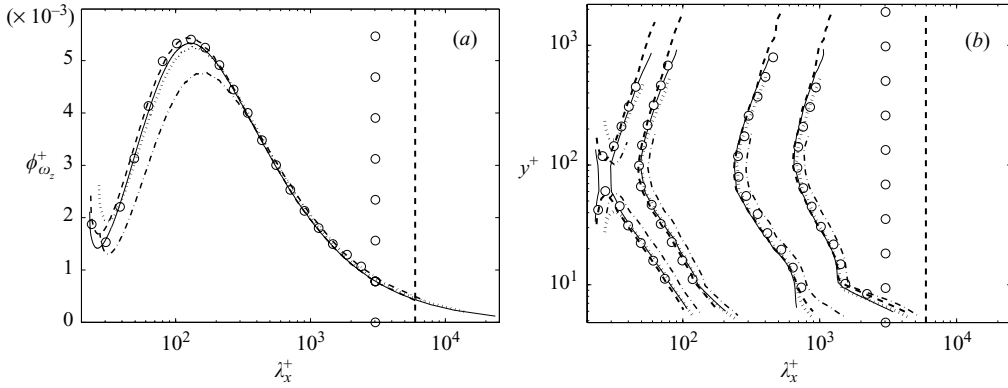


FIGURE 1. Streamwise enstrophy spectral densities  $\phi_{\omega_z}$  of the spanwise vorticity. (a) Represented as functions of the streamwise wavelength  $\lambda_x$  and expressed in wall units, at  $y^+ = 50$ . (b) Represented as functions of  $\lambda_x$  and of  $y$  and normalized with  $\omega_z^2(y)$ . The contours by pairs from inside to outside are isolines of 1/3 and 2/3 of the maximum value from case L950. The vertical lines mark the lengths of the boxes for cases S950 and S1900. Lines and symbols as in table 1.

that the streamwise resolution of  $\omega_z$  is worst at  $y^+ \approx 80$ . The spanwise resolution of  $\omega_y$  is worst at  $y^+ \approx 40$ .

Although the small numerical box of case S950 interferes with the large velocity structures of the outer region (del Álamo *et al.* 2004), the enstrophy-containing scales are not affected by the finite size of the box, as shown by the agreement between cases S950 and L950 in figure 1. The same is expected to happen for case S1900, whose box is approximately twice as large in wall units as that of S950.

The time step of the simulations was chosen to keep the CFL number at 0.5. However, because of a bug discovered in the code late in the post-processing phase, about 1% of the points in the neighbourhood of  $y^+ = 20$  probably ran at CFLs which might have reached about unity in the worst case of the highest Reynolds number. The stability limit of the Runge–Kutta is about  $\text{CFL} = 4$  in that region. The cases S1900 and L950 were run for an extra half washout with the correct CFL limit. No change was observed in the statistics.

### 3. Vortex identification and classification

This section describes the procedures employed to identify and to classify vortex clusters in the present flows. Our method is based on the discriminant criterion of Chong, Perry & Cantwell (1990), which was first applied using constant non-zero thresholds to study wall turbulence structure by Blackburn *et al.* (1996) and Chong *et al.* (1998). Here, we introduce a non-uniform threshold that allows us to compare systematically data from different wall distances. We also derive a way to compute the lowest possible threshold that allows the identification of individual vortices. In §3.1, the vortices extracted with the present method are characterized in terms of their radii and azimuthal velocities, which are compared to similar data available in the literature.

According to Chong *et al.* (1990), a vortex core is a region where the velocity gradient tensor  $\nabla \mathbf{u}$  is dominated by its rotational part. Expressed in terms of the discriminant of  $\nabla \mathbf{u}$ , this condition is  $D > 0$ . It is beyond the scope of this paper to compare carefully the vortex eduction methods available in the literature, and the

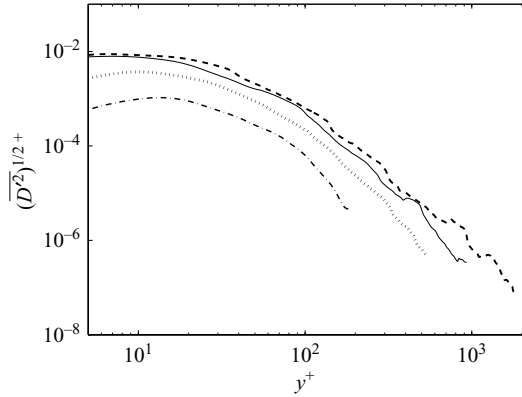


FIGURE 2. Standard deviation  $(\overline{D^2})^{1/2}$  of the discriminant of the velocity gradient tensor, normalized in inner units and represented as a function of the wall distance  $y$ . Lines and symbols as in table 1.

reader is referred to the paper of Cucitore, Quadrio & Baron (1999) for a detailed description of the most popular ones. Chakraborty, Balachandar & Adrian (2005) showed that all these methods are approximately equivalent, which strongly suggests that the choice of a particular criterion does not affect the present results.

Nevertheless, the dependence of the identification methods on their thresholds becomes troublesome for wall-bounded turbulence, owing to the inhomogeneity of the flow in the wall-normal direction. It complicates the comparison of data from different wall distances when a uniform threshold is used. When the threshold is chosen to visualize properly the vortices of the near-wall layer of the present channels, very few of them are observed in the outer region. Conversely, when the threshold is lowered to visualize the vortices of the outer layer, the near-wall region becomes confusingly cluttered with vortex tubes. This behaviour, which agrees in general with the observations of Blackburn *et al.* (1996), worsens with increasing Reynolds number. Nagaosa & Handler (2003) found similar effects using the  $Q$  criterion of Hunt, Wray & Moin (1988) with uniform thresholds, but they pointed out that the p.d.f. of the second invariant normalized with its standard deviation,  $Q/(\overline{Q^2})^{1/2}$ , is homogeneous everywhere except in the viscous sublayer. Based on this result, they proposed that the threshold should vary with wall distance as  $(\overline{Q^2})^{1/2}$ . We will show below that the same is roughly true for the  $D$  criterion.

Following this argument we consider that a point  $\mathbf{x}$  belongs to a vortex if

$$D(\mathbf{x}) > \alpha \overline{D^2(y)}^{1/2}, \quad (3.1)$$

where  $\alpha$  is the actual thresholding parameter and  $(\overline{D^2})^{1/2}$  is the standard deviation of  $D$  over wall-parallel planes, shown in figure 2 for the present channels. This procedure palliates the problem of inhomogeneity, and yields a vortex volume fraction which depends on  $y$  much less than the one obtained using a uniform threshold. This is shown in figure 3(a), which displays the relative volume  $V_r$  occupied by the points satisfying (3.1) as a function of  $\alpha$  and of the wall distance. The variation of  $V_r$  for a given threshold, from its peak at  $y^+ \approx 30$  to the centre of the channel is negligible compared to the variation of  $(\overline{D^2})^{1/2}$  in figure 2. While the latter varies by a factor  $O(10^3-10^5)$  across the channel, depending on the Reynolds number, the former changes by less than 4. Thus, in the representation of figure 3(a), using a uniform threshold would

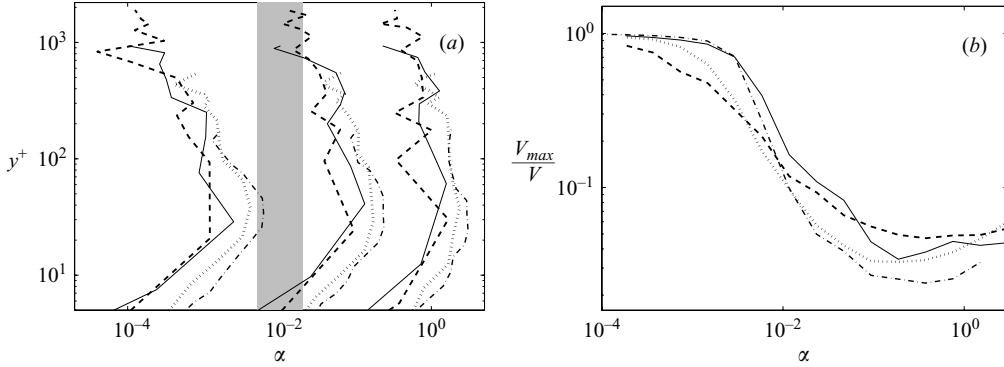


FIGURE 3. (a) Relative volume  $V_r$  occupied by the points satisfying criterion (3.1), represented as a function of the threshold  $\alpha$  and of the wall distance  $y$ . The contours are from right to left  $10^{-3}(\times 10)10^{-1}$ . The shaded region marks the location of the percolation crisis. (b) Volume  $V_{max}$  of the largest cluster normalized with the overall volume  $V$  occupied by all the clusters, represented as a function of the threshold  $\alpha$ . Lines and symbols as in table 1.

be equivalent to increasing  $\alpha$  by a factor of up to  $10^5$  from the near-wall region to the channel centre. That is the range of the horizontal axis in the figure. Notice also that the collapse of the contours from the different channels indicates that the fraction of volume occupied by the vortices identified following (3.1) depends little on the Reynolds number.

Yet, the present identification method depends on the parameter  $\alpha$ . In principle, we would like to use the theoretical criterion  $D > 0$ , but it is known that the zero threshold leads to confusing results in which all the vortices merge into a few complex objects (Blackburn *et al.* 1996). Here we present a way to find the lowest practical threshold for which the vortices can still be identified individually. For a given  $\alpha$ , each set of connected points satisfying the criterion (3.1) is merged and classified as an individual object. Connectivity is defined by the six orthogonal nearest neighbours of each grid point.

Figure 3(b) represents the ratio between the volume of the largest cluster  $V_{max}$  and the overall volume  $V$  occupied by the clusters. When  $\alpha \approx 1$ , only a few small objects are identified. With decreasing  $\alpha$ , new clusters appear while others coalesce, and the variation of  $V_{max}/V$  with  $\alpha$  is the result of the trade-off between the two processes. Figure 3(b) shows that they are balanced above  $\alpha \approx 10^{-2}$ , so that  $V_{max}/V$  remains roughly constant while the number of clusters increases. Below that critical value of  $\alpha$ , few new clusters are identified and the existing ones keep merging until only a single large, sponge-looking object remains, yielding  $V_{max} = V$ . Moisy & Jiménez (2004) observed a similar behaviour in isotropic turbulence using the modulus of vorticity as the threshold. They described it using the analogy of a percolation transition in which, given the connectivity rules, an infinite cluster appears above a given volume density. The phenomenon of percolation is common to many physical processes in which a property communicates through a randomly distributed medium (Stauffer 1985). Here, it imposes a natural limitation on  $\alpha$  which is intrinsic to the geometrical configuration of the vortices in the flow.

The percolation threshold, defined as the value of  $\alpha$  for which the slope of  $V_{max}/V$  is maximum, occurs at  $\alpha_c \approx 0.008$  in the present channels regardless of the Reynolds number. Such a low value of  $\alpha_c$  should not be surprising considering that  $D$  is a sixth-order function of the velocity gradient. The threshold that has been used in this

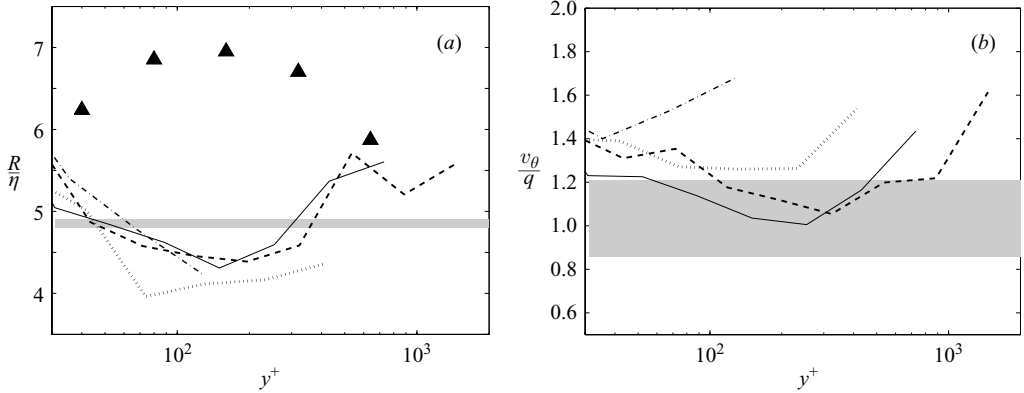


FIGURE 4. (a) Average 1/e vortex radius  $R$  non-dimensionalized with the local Kolmogorov scale  $\eta$ , and represented as a function of the wall distance  $y$ .  $\blacktriangle$ ,  $Re_\tau = 800$  channel (Tanahashi *et al.* 2003, 2004). (b) Average maximum azimuthal velocity  $v_\theta$  of the vortices normalized with the local turbulent intensity  $q$ , and represented as a function of  $y$ . The value of the threshold used in (3.1) is  $\alpha \approx 2.5\alpha_c$ . Lines and symbols as in table 1. The shaded patches cover the maximum scatter of  $R$  and  $v_\theta$  in isotropic turbulence up to  $Re_\lambda = 170$  (Jiménez & Wray 1998).

paper as a reference is  $\alpha = 0.02 \approx 2.5\alpha_c$ , which lies slightly above the beginning of the percolation transition in figure 3(b). The influence of this choice will be considered later.

Because of the high cost of the clustering algorithm at low  $\alpha$  we have used sub-boxes of size  $l_x^+ \times l_y^+ \times l_z^+ \approx 2000 \times 2Re_\tau \times 1000$  instead of the full fields to produce figure 3(b). The location of the percolation crisis should not be affected by this, since the volume occupied by the largest cluster at  $\alpha = \alpha_c$  is less than 10% of the volume of the sub-box in all the cases. The full boxes have been employed for the rest of the results in this paper. The number of fields that has been used from each simulation, and the corresponding number of clusters that have been identified at  $\alpha \approx 2.5\alpha_c$ , are indicated in table 1. According to our experience, these are enough to provide good convergence for the statistics that are presented in the following sections.

### 3.1. Properties of individual vortices

For simplicity, the properties of the vortex cores extracted using the above procedure have been studied analysing sections of spanwise vortices in  $(x, y)$ -planes. These sections are roughly representative of the whole vortex population everywhere except in the buffer layer, where the flow is most anisotropic. They are identified as sets of connected points satisfying (3.1) and whose vorticity vector is inclined less than  $30^\circ$  to the  $z$ -direction. The influence of the threshold on the clustering of these objects is similar to the three-dimensional case, but in the  $(x, y)$ -planes the percolation crisis occurs at  $\alpha \approx 10^{-4}$ .

We characterize the spanwise vortex sections by fitting their vorticity distribution to that of an elliptical Gaussian vortex, as in Jiménez *et al.* (1993). The principal semi-axes  $a$  and  $b$  of each vortex, and its 1/e radius,  $R = (ab)^{1/2}$ , are obtained from the tensor of inertia of the local vorticity distribution, taking into account its angle with the  $(x, y)$ -plane. The maximum azimuthal velocity given by the Gaussian model is  $v_\theta = 0.203\Gamma/(a + b)$ , where  $\Gamma$  is the circulation obtained from the integral of  $\omega_z$  inside the vortex section.

Figures 4(a) and 4(b) show that  $R$  and  $v_\theta$  depend little on  $Re_\tau$  and  $y$ , when normalized with the Kolmogorov scale  $\eta$  and with the r.m.s. turbulent intensity



$q = [(\overline{u^2} + \overline{v^2} + \overline{w^2})/3]^{1/2}$ . Their numerical values agree reasonably with those obtained by Jiménez & Wray (1998) in isotropic turbulence up to  $Re_\lambda = 170$ . The present vortices are, however, about 20 % thinner and twice as strong as those extracted by Tanahashi *et al.* (2003, 2004) in channels up to  $Re_\tau = 800$ . This can be explained considering that the criterion (3.1) detects only the most intense vortices, while that used by Tanahashi *et al.* (2003, 2004), not requiring a threshold, does not discriminate between weak and strong objects. Consistently, the fraction of volume occupied by the vortices in the present channels, 2–3 % for  $\alpha \approx 2.5\alpha_c$ , is much lower than the 39 % obtained in isotropic turbulence by (Tanahashi *et al.* 1997), using the method of Tanahashi *et al.* (2003, 2004). The same conclusion is drawn comparing results from isotropic turbulence at similar Reynolds numbers. The azimuthal velocities reported by Jiménez & Wray (1988) for the most intense vortices occupying 1 % of the flow volume, are nearly twice as high as those obtained by Kida, Goto & Makihara (2002) using  $Q > 0$ , which yields a volume fraction of 40 %.

#### 4. Vortex clusters

This section studies the properties of the vortex clusters found in the logarithmic and outer regions of our channels. In §4.1, we will show that their population is separated into two families. The first one is composed of small individuals that are detached from the wall and the second one is formed by taller objects that reach the near-wall region.

We will focus on these tall attached clusters in §4.2. They form a self-similar range that links the small scales near the wall to the larger ones far from it. In §4.2.1, we will see that the lengths and widths of these objects are proportional to the wall distance of their centres, and comparable to the local integral scale of the flow,  $\overline{u^3}/\varepsilon$ . The influence of the tall attached clusters on the outer region is analysed in §4.2.2. We will see that it depends on the vortex identification threshold and becomes independent of the Reynolds number for low-enough thresholds.

The organization of the turbulent velocity fluctuations associated to the tall attached clusters is studied in §4.2.3. The results will indicate that, while the average structure of these objects coincides with a large-scale hairpin eddy, their instantaneous configuration is very complex.

In §4.2.4, we will see that the average velocity field conditioned to the presence of the tall attached clusters shows very large  $u$ -structures, whose average geometry is consistent with a cone tangent to the wall along the  $x$ -axis. We will interpret these structures as ‘wakes’ that the clusters leave behind them as they move with the flow. The spreading of the wakes will be shown to agree with a linear advection–diffusion model in which the diffusion is produced by the incoherent background turbulence. By analysing the lifetimes of the clusters and the lengths of the conditional wakes, we conclude that the clusters are triggered by older wakes in front of them, and that hence the clusters and the wakes are involved in a cycle of mutual regeneration.

Finally, the properties of the detached clusters will be presented in §4.3.

##### 4.1. Attached and detached clusters

Figure 5 shows the volume  $p_V$  contained in clusters whose minimum and maximum wall distances, measured from the wall closest to their centres, are  $y_{min}$  and  $y_{max}$ . By definition  $y_{max} > y_{min}$ , so that  $p_V$  can only be non-zero above  $y_{max} = y_{min}$ . For a spatially homogeneous distribution of vortex clusters  $p_V$  would only depend on  $y_{max} - y_{min}$ , which is not the case for the present channels. In particular, figure 5 reveals that  $p_V$

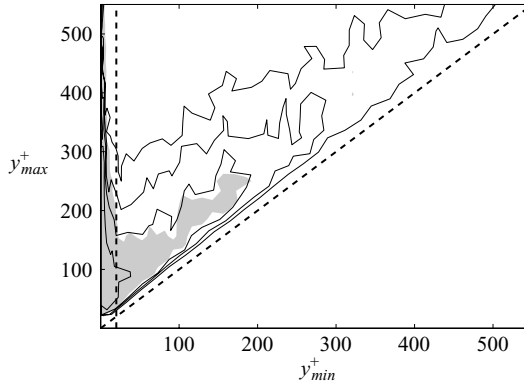


FIGURE 5. Volume distribution  $p_V$  of the clusters as a function of their minimum  $y_{min}$  and maximum  $y_{max}$  wall distances. Case L550. The line contours come from  $\alpha \approx 2.5\alpha_c$  and contain 20, 40, 60 and 80 % of the data. The shaded contour comes from  $\alpha \approx \alpha_c$  and contains 40 % of the data. The vertical dashed line is  $y_{min}^+ = 20$ . The diagonal dashed line is  $y_{max} = y_{min}$ .

peaks in the buffer layer in agreement with figure 3(a), and its shape suggests that the population of clusters may be divided into two families according to their wall-normal position and to their height. The first family corresponds to the inclined band that occupies most of the area of figure 5. It is formed by vortex packets that reside far from the wall, and is almost spatially homogeneous according to the argument above. We call them wall-detached clusters. The second family is the narrow vertical band to the left of the line representing  $y_{min}^+ \approx 20$ . It consists of clusters which are tall, but which reach into the near-wall region. We call them wall-attached clusters. They are important, even if few, because of their large sizes.

The data in figure 5 come from case L550 to facilitate the visualization of the narrow band corresponding to the tall attached clusters, but similar results are obtained for the remaining Reynolds numbers. The general structure of  $p_V$  does not vary with the threshold for  $\alpha \gtrsim \alpha_c$ . When  $\alpha$  decreases, new small clusters appear near  $y_{min} = y_{max}$ , and compensate the migration away from that region caused by the merging of some of the previously existing objects. As a result, the volume occupied by the clusters increases everywhere in the  $(y_{min}, y_{max})$ -plane and  $p_V$  keeps its shape approximately. An example is included in figure 5. However, when  $\alpha$  crosses the percolation transition, cluster aggregation becomes dominant and the whole distribution accumulates rapidly at  $(y_{min}, y_{max}) \approx (0, 2h)$ .

The vortex clusters of several realizations from each of the present channels have been visualized plotting the isosurfaces  $D = \alpha [D^2(y)]^{1/2}$ , consistent with the identification criterion (3.1). In agreement with the discussion in §3, the resulting vortex fields are more densely populated in the logarithmic and outer regions than those obtained by Blackburn *et al.* (1996) and by Chong *et al.* (1998) using isosurfaces of uniform  $D$ . Because of this, the visualizations of full fields are extremely cluttered, and it is difficult to extract conclusions from them.

Considering individual objects is easier and can be done systematically, since the clusters have been isolated and classified. Proceeding in this way it is found that the wall-detached clusters cover a wide spectrum of shapes, which are reminiscent of the worms of isotropic turbulence. They range from single vortex tubes to complex bundles of tangled filaments. Figure 6(a) is an example of medium complexity, taken from an snapshot of case S1900 (for comparison see figure 6 in Moisy & Jiménez 2004).

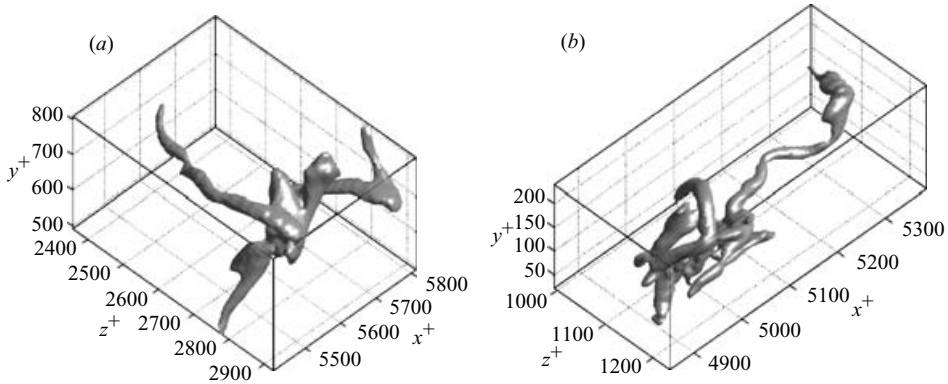


FIGURE 6. Three-dimensional clusters from case S1900,  $\alpha \approx 2.5\alpha_c$ . (a) Representative detached cluster. (b) Representative tall attached cluster.

Most of the wall-attached clusters turn out to be single near-wall quasi-streamwise vortices, but there is an appreciable number of ‘tall’, more complex clusters that penetrate in the logarithmic region, in agreement with figure 5. The former have been studied thoroughly and are known to generate velocity fluctuations at all length scales in the buffer layer (Robinson 1991a; Jiménez *et al.* 2004). In this paper, we pay especial attention to the latter.

Little can be said in general about the shape of the tall attached clusters, except that they are usually inclined upward and along the streamwise direction. They sometimes contain one or several more-or-less-clear specimens of the vortex loops that have been discussed since Theodorsen (1952) by many workers (Head & Bandyopadhyay 1981; Perry & Chong 1982; Acarlar & Smith 1987; Adrian *et al.* 2000), and that were observed previously in diverse numerically simulated turbulent wall flows (Moin & Kim 1985; Robinson 1991b). That is the case of figure 6(b), which has been extracted from the same flow realization as figure 6(a). Nevertheless, there are many other configurations, more complex and less eye-catching than vortex loops or than other kinds of simple organized structures. Those configurations appear more often in the larger clusters. They cannot be classified visually and have to be described statistically.

To compute statistics separately for detached clusters, attached clusters and tall attached clusters, we must define these groups mathematically. Based on figure 5, we will consider that those clusters with  $y_{min}^+ \geq 20$  are detached and that those with  $y_{min}^+ < 20$  are attached. Among the latter, those with  $y_{max}^+ > 100$  will be tall attached clusters.

## 4.2. Tall attached clusters

### 4.2.1. Scaling

The scaling of the tall attached clusters has been analysed by inscribing each of them into a parallelepipedal box aligned with the Cartesian grid, and by comparing the dimensions  $\Delta_x$ ,  $\Delta_z$  and  $\Delta_y$  of the boxes with the distances  $y_c$  from their centres to the wall. Figures 7(a) and 7(b) display the joint p.d.f.s of the logarithms of the wall-parallel dimensions of the boxes and of  $y_c$ . These magnitudes measure the number of clusters per unit area of the logarithmic representation of the figure. Since we are more interested in the tall attached clusters than in the buffer-layer ones, only those objects whose vortex volume is larger than  $30^3$  wall units have been considered. The

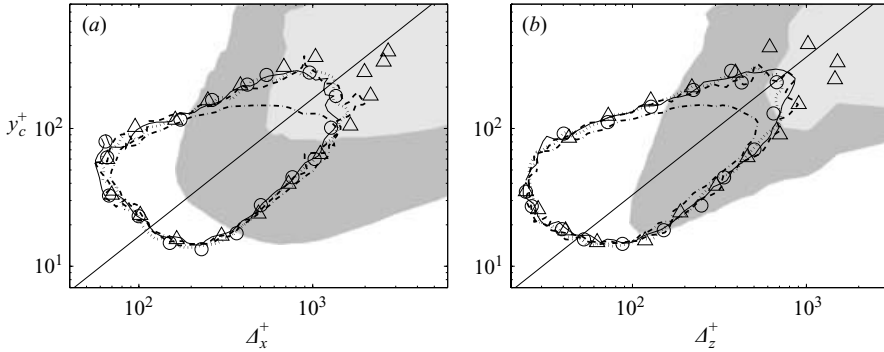


FIGURE 7. Probability density functions of the logarithms of the size  $\Delta$  of the attached clusters, and of the wall distances  $y_c$  of their centres. The lines and symbols of table 1 have been obtained using  $\alpha \approx 2.5\alpha_c$  in (3.1);  $\triangle$ , case S1900,  $\alpha \approx \alpha_c$ . The iso-probability contours contain 98 % of the data; the shaded contours are the cospectrum  $\phi_{uv}$  and represent 1/20 and 1/5 of its maximum value; we have used the correspondence  $\lambda \approx \Delta$  and  $y_c \approx y/2$ . (a)  $p(\log \Delta_x, \log y_c)$  and  $\phi_{uv}(\lambda_x, y)$ ; the solid straight line is  $\Delta_x = 6y_c$ . (b)  $p(\log \Delta_z, \log y_c)$  and  $\phi_{uv}(\lambda_z, y)$ ; the solid straight line is  $\Delta_z = 3y_c$ .

p.d.f.s are organized along

$$\Delta_x \approx 6y_c, \quad \Delta_z \approx 3y_c, \quad (4.1)$$

providing direct evidence of the self-similarity of the lengths and widths of the tall attached clusters with respect to the wall distances of their centres. They support the existence of the hierarchy of scales postulated by Perry & Chong (1982) and which is the essence of developed turbulence. Note that since  $y_{max} \gg y_{min}$  for the tall attached clusters,  $y_c \approx \Delta_y/2$ , and (4.1) also implies that the lengths and widths of these objects are proportional to  $\Delta_y$ . Figures 7(a) and 7(b) show that the same scalings are obtained for other values of the identification threshold.

The shaded contours in figure 7(a) are the spectral densities of the shear Reynolds stress,  $\phi_{uv}(\lambda_x, y) = k_x y \int Re(\widehat{u\bar{v}}^*) dk_z$ , from case S1900, and those in figure 7(b) are  $\phi_{uv}(\lambda_z, y)$ . These contours show the wavelengths and wall distances associated to  $\overline{u\bar{v}}$ -containing motions. To compare  $\phi_{uv}$  with the p.d.f.s of the sizes of the attached clusters, it is convenient to use the correspondence  $y \approx y_c/2$ . The reason is that  $\phi_{uv}(\lambda, y)$  contains contributions from all the attached clusters that intercept the wall distance  $y$ , which are those with  $y_c > y/2$ . Since, as we will see, the number of tall attached clusters decreases rapidly with  $y_c$ , their effect on the  $uv$ -cospectrum is dominated by the lowest of those clusters, with  $y_c = y/2$ . The p.d.f.s of figures 7(a) and 7(b) agree reasonably well with  $\phi_{uv}$ , suggesting a relation between the tall attached clusters and the organization of the velocity field in the overlap region, which will be explored below in more detail. The fact that the agreement is not perfect should not be surprising, considering that the correspondence between  $y_c$  and  $y/2$  is only approximate, and that sizes and spectral wavelengths are proportional, but not identical (Jiménez *et al.* 2004).

The coincidence of the sizes of the clusters with the scales of the Reynolds stresses suggests that some properties of these objects, such as their size, may be dominated by their associated velocity structures instead of by their constituent vortices. This possibility has been tested by analysing the clusters in low-pass filtered fields, in which the individual vortices are smoothed, and what remains is only the integrated circulation over fairly large scales. In each direction of the original grid, a box filter of

Filter	Symbol	$\delta_x^+$	$\delta_z^+$	$\delta_y^+$	$\alpha_c$	$N_F$	$N_C$
F1	...▲...	48	24	20	0.06	42	$2.4 \times 10^5$
F2	...■...	96	48	40	0.12	42	$6.4 \times 10^4$
F3	...●...	192	96	40	0.24	47	$2.2 \times 10^4$

TABLE 2. Parameters of the box filters used in case S1900.  $\delta_x$ ,  $\delta_z$  and  $\delta_y$  are the filter widths.  $\alpha_c$  is the percolation value of the identification threshold.  $N_F$  is the number of fields used to accumulate statistics and  $N_C$  is the number of clusters that have been identified at  $\alpha \approx 2.5\alpha_c$ .

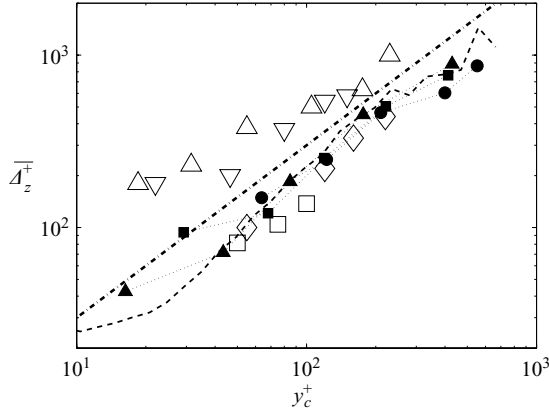


FIGURE 8. Average widths  $\overline{\Delta}_z$  of the attached-cluster boxes as functions of the distance  $y_c$  from their centres to the wall. Case S1900,  $\alpha \approx 2.5\alpha_c$ , lines and symbols as in tables 1 and 2. — —,  $\overline{\Delta}_z = 3y_c$ . The open triangles are the widths of the ejections in laboratory open channels (Nakagawa & Nezu 1981);  $\nabla$ ,  $Re_\tau = 318$ ;  $\triangle$ ,  $Re_\tau = 696$ . The rest of the data are the widths of hairpin packet signatures in laboratory boundary layers;  $\square$ ,  $Re_\theta = 2500$  (Ganapathisubramani *et al.* 2003);  $\diamond$ ,  $Re_\theta = 7705$  (Tomkins & Adrian 2003).

uniform width  $\delta$  and half-window overlap is applied to  $\nabla \mathbf{u}$ , and the result is sampled on a grid of size  $\delta/2$ , on which  $D$  is calculated. The discriminant of the filtered fields is processed as described in §3 to identify and classify vortex clusters. Figure 5 indicates that a wall-normal resolution finer than a few tens of wall units is required to distinguish the attached clusters from the detached ones, which introduces an upper bound on the wall-normal width of the filter. A certain degree of grid isotropy has to be preserved, which also limits the filter widths in the wall-parallel directions. We have used the three filters described in table 2.

The average widths  $\overline{\Delta}_z$  of the attached clusters from the filtered fields of case S1900 have been represented in figure 8. They agree with those coming from the fully resolved case for  $\overline{\Delta}_z \gtrsim 2\delta_z$ , whereas the narrower clusters are affected by the filter. Similar results are obtained for the average lengths of the clusters, suggesting that the self-similar scaling (4.1) is determined by the velocity eddies that accompany the clusters, instead of by their fine-scale vortices. This offers an explanation for the agreement of the sizes of the present clusters and those of the hairpin packet signatures of laboratory experiments, which are usually obtained from measurements at relatively coarse resolution. The laboratory results have been represented in figure 8 using the relation  $y_c = y/2$ , because they are taken at fixed  $y$ . The agreement is especially good for the widths of Ganapathisubramani *et al.* (2003) and of Tomkins & Adrian (2003),

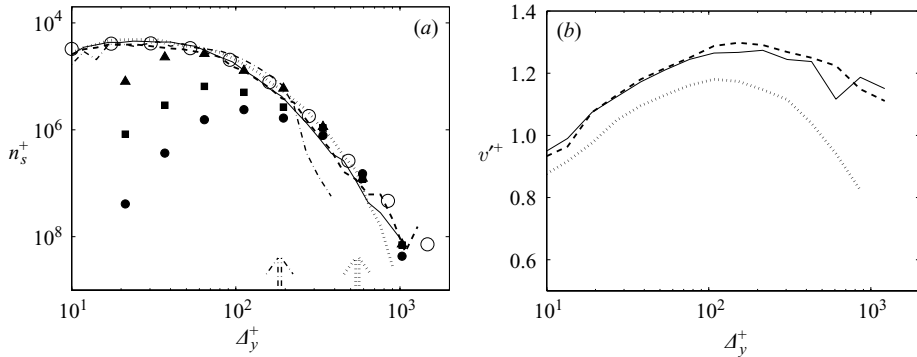


FIGURE 9. (a) Densities  $n_s$  of attached clusters represented as functions of their height,  $\Delta_y$ . The vertical arrows indicate the half-widths of the two lowest-Reynolds-number channels. (b) Root mean squares  $v^{r+}$  of the wall-normal velocity in the  $(x, z)$ -planes bisecting boxes of the attached clusters, represented as functions of  $\Delta_y$ . The threshold used in (3.1) is  $\alpha \approx 2.5\alpha_c$ . Lines and symbols as in tables 1 and 2.

which were measured directly on instantaneous and conditionally averaged hairpin packet signatures. Nakagawa & Nezu (1981) assumed a log-normal distribution for  $\Delta_z$ , and fitted it to their previous observations (Nakagawa & Nezu 1977) and to the short-separation behaviour of the spanwise auto-correlation function of  $u$ . Their results show the same linear dependence on  $y$  as the rest of the data in figure 8, but they are approximately twice as wide. This discrepancy is probably due to the different analytical procedures employed.

#### 4.2.2. Maximum heights

An interesting question is whether the velocity structures that we have associated with the tall attached clusters are features of the whole outer region, or whether they just appear in the lower edge of the logarithmic layer. Zagarola & Smits (1998) observed that the properties of the mean profile in the overlap region of their very high-Reynolds-number pipe flow change around  $y^+ = 500$ , which could imply that some buffer-layer phenomena persist to that height and become negligible for most of the logarithmic layer at high enough  $Re_\tau$ . However, some of the signatures of hairpin packets observed in other laboratory experiments at  $Re_\tau$  of the order of a few thousands conserve their spatial coherence across the whole overlap region (Head & Bandyopadhyay 1981; Adrian *et al.* 2000). The presence of attached vortex loops in the outer region of numerically simulated wall flows at  $Re_\tau = O(100)$  has often been reported (Moin & Kim 1985; Robinson 1991*b*; Chong *et al.* 1998). At the limited Reynolds numbers of both numerical and laboratory experiments, it is difficult to decide from qualitative observations how the distribution of attached clusters will evolve as  $Re_\tau$  increases. Here we try to shed some light on that question by studying the distribution of the cluster heights.

Figure 9(a) displays the densities of attached clusters per unit height  $\Delta_y$ , and per unit wall-parallel area,  $n_s = N(\Delta_y)/(L_x L_z)$ , where  $N$  is the histogram of  $\Delta_y$ . These magnitudes peak in the buffer layer owing to the contribution of the dense population of vortices in that region, but here we focus on their tails at high  $\Delta_y$ . Since  $\Delta_y \approx 2y_c$  for the tall attached clusters, those tails are similar to the integrals of the p.d.f.s in figures 7(a) and 7(b) along the corresponding wall-parallel direction, but here we are representing absolute cluster numbers, not normalized p.d.f.s.

The data from the low-pass filtered fields of case S1900, also included in figure 9(a), coincide with the fully resolved data above  $\Delta_y \approx 3\delta_z$ , and the same happens when the filters are applied to the rest of the present flows. This result suggests that  $n_s$  also measures the volume density of tall attached velocity eddies, because the number of identified objects does not change even when the vortices that constitute the clusters are progressively smoothed out by coarsening the filter. It also suggests that the tails of  $n_s$  at high  $\Delta_y$  are not contaminated by artefacts of the identification method or of the clustering algorithm at scales smaller than the widths of the filters.

The influence of the clusters on the outer region, and hence that of their associated velocity structures, can be measured by studying the variation with  $Re_\tau$  of their contribution to the Reynolds stresses at constant  $y/h$ . This is equivalent to analysing the fraction of the area  $S$  covered by them in the wall-parallel plane,  $F_s = S/(L_x L_z)$ , because their associated turbulent intensities scale on average with  $u_\tau$  and depend little on  $\Delta_y$ , as shown in figure 9(b). The scalings (4.1) imply that  $\Delta_x \Delta_z \approx 4.5 \Delta_y^2$ , so

$$F_s(y^+) \sim \int_{y^+}^{Re_\tau} \Delta_y^2 n_s^+(\Delta_y) d\Delta_y. \quad (4.2)$$

Notice that  $F_s$  also indicates the relative volume occupied by the cluster boxes at a given wall distance. Assuming that  $n_s^+(\Delta_y^+) \sim (\Delta_y^+)^{\beta}$  with  $\beta \neq -3$ , we have

$$F_s \sim Re_\tau^{\beta+3} [1 - (y/h)^{\beta+3}] / (\beta + 3). \quad (4.3)$$

Only if  $n_s$  decays faster than  $\Delta_y^{-3}$ , does the contribution of the attached clusters to the Reynolds stresses decrease with  $Re_\tau$  for constant  $y/h$ . For the limiting value  $\beta = -3$ , the integral in (4.2) yields  $F_s \sim \log(h/y)$  and the influence of the attached clusters on the outer region becomes independent of the Reynolds number. In that case, the volume density of these objects is self-similar and scales both in wall and in outer units.

In the present flows, each value of the identification threshold corresponds to a set of clusters, whose influence on the outer region is measured by its associated decay exponent,  $\beta(\alpha)$ . Consistent with criterion (3.1), that influence should increase with decreasing the threshold, because the set of clusters extracted for a given threshold  $\alpha_0$  is a subset of those obtained for  $\alpha > \alpha_0$ . This behaviour can be observed in figure 10, which shows the average logarithmic slope of  $n_s$  above  $\Delta_y^+ = 100$ . This magnitude is a reasonable approximation to the decay exponent  $\beta$ , since the slopes of the curves in figure 9(a) are roughly uniform above that level. Figure 10 indicates that  $\beta$  is only a function of  $\alpha/\alpha_c$ , both for the full fields at the three Reynolds numbers and for the coarsest filter of case S1900. In the filtered case,  $\beta$  has been computed for  $\Delta_y^+ > 300$  because the filter size interferes with the clusters below that level. The same results are obtained for the remaining combinations of present filters and Reynolds numbers, suggesting that the conclusions inferred by comparing fully resolved data with filtered data in figure 9(a) apply regardless of the identification threshold.

Figure 10 shows that the decay exponent of  $n_s$  reaches the limit value  $\beta = -3$  around the percolation threshold. If  $\alpha$  is decreased below that level,  $n_s$  develops a ‘bump’ around  $\Delta_y = h$ , but its slope in the logarithmic region does not vary appreciably. Thus, the maximal set of tall attached clusters observed in the present flows has  $\beta = -3$ , and its influence on the outer region is independent of the Reynolds number according to the discussion above. This maximal set is actually the ‘full’ set of wall-attached eddies because it fills a fraction of volume of order unity in our channels. The computed

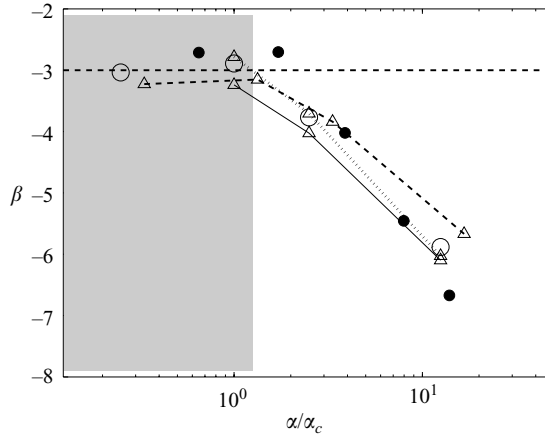


FIGURE 10. Logarithmic slope  $\beta$  of  $n_s(\Delta_y)$  as a function of the identification threshold  $\alpha/\alpha_c$ . The lines have been plotted to aid the eye and only the symbols correspond to data points. Lines and symbols as in tables 1 and 2. The shaded area marks the percolated range. The horizontal line is  $\beta = -3$ .

relative volumes occupied by the tall attached clusters in our channels vary between 0.18 and 0.83 for  $\alpha \approx \alpha_c$ .

The saturation of  $\beta$  for  $\alpha < \alpha_c$  can be explained with the help of (4.3), which indicates that  $F_s$  decreases as a negative power of  $y$  for  $\beta < -3$ , but only algebraically for  $\beta > -3$ . In both cases, the relative volume of the cluster boxes is maximum for  $y/h \rightarrow 0$ , suggesting that the process of percolation would start near the wall in any flow realization. Below  $\beta = -3$ , the propagation of percolation away from the wall is prevented by the rapid decrease with  $y$  of the volume occupied by the cluster boxes, but the same does not happen above that limit. Hence, if the clusters in a given realization reach  $\beta > -3$  when the threshold is lowered, they will percolate completely and become part of the ‘bump’ of  $n_s$  around  $\Delta_y = h$  that was described above as indicative of the percolation regime.

The variation of the number of signatures of hairpin packets found by Ganapathisubramani *et al.* (2003) between  $y^+ = 92$  and  $y^+ = 198$  yields  $\beta \approx -3.13$ , suggesting that the influence of those packets also reaches the outer region of their boundary layer ( $Re_\tau = 1060$ ). However, these authors hardly observed hairpin packet signatures at  $y^+ \approx 500$ , and concluded that their influence should not remain important above the logarithmic layer. Figures 7(a) and 7(b) suggest an explanation for this discrepancy. They show that the sizes of the clusters that intercept  $y^+ = 500$  are comparable to the dimensions of the field of view used by Ganapathisubramani *et al.* (2003),  $L_x^+ \times L_z^+ \approx 1300 \times 1300$ , which should affect their feature extraction algorithm. Besides, using the number of clusters that intercept a given  $y$  as a diagnostic of their influence on the outer region may not be accurate, because the taller clusters are also larger, and they contribute to the Reynolds stresses more than the smaller ones. Notice, in fact, that the relative volume occupied by the cluster boxes decays only logarithmically with  $y$  for  $\beta = -3$ , even if the number of clusters that intercept a given wall distance falls as  $y^{-2}$ .

The velocity fluctuations associated with the tall attached clusters are stronger than their background, and this causes the percolation of their constituent vortices down to the wall. We have seen in figures 4(a) and 4(b) that the radii of individual vortices



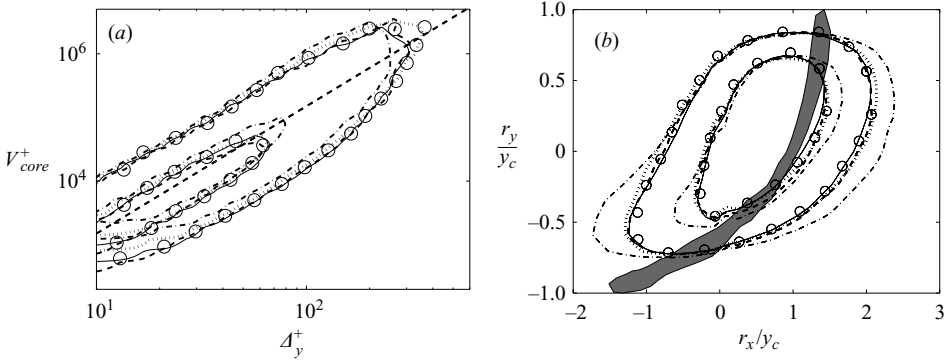


FIGURE 11. (a) Probability density functions of the logarithms of the volume  $V_{core}$  occupied by the vortices in the attached clusters, and of the cluster height  $\Delta_y$ . The levels represented contain 50 % and 98 % of the data. The straight dashed line has a logarithmic slope of 2. (b) Probability density functions of the streamwise  $r_x$  and wall-normal  $r_y$  positions of the vortex points of the tall attached clusters, normalized with the wall distances  $y_c$  of their centres. The levels represented contain 33 % and 66 % of the data. The dark patch is a side-view of a hairpin vortex taken from Haidari & Smith (1994). Lines and symbols as in table 1. The threshold used in (3.1) is  $\alpha \approx 2.5\alpha_c$ .

are proportional to  $\eta \sim (v^3/\varepsilon)^{1/4}$ , and that their azimuthal velocity scales with the local turbulence intensity  $q$ . Assuming that the vortices of the tall attached clusters have to dissipate the energy flux injected by their associated velocity eddies, we obtain  $\varepsilon \sim q_c^3/y_c$ , where  $q_c$  is the intensity of those eddies. The discriminant in those vortices,  $D \sim (q_c/\eta)^6$ , is then expected to be  $(q_c/q)^{21/2}$  times higher than in the background. Accordingly, the percolation threshold for the vortices of the tall attached clusters would be lower than in the background by the same factor. For the present clusters, it is indeed true that  $q_c/q \approx (\alpha/\alpha_c)^{2/21}$ , which suggests that these vortical structures are just markers of especially intense eddies at the integral scale, and that they are identified because of their higher dissipation.

#### 4.2.3. Organization and structure

The scalings in (4.1) imply that the volume  $\Delta_x \Delta_y \Delta_z$  of the boxes that bound the tall attached clusters grows as  $\Delta_y^3$ . The same is not true for the volume of their vortex cores, which grows approximately as  $\Delta_y^2$  as shown in the p.d.f.s of figure 11(a). Although only one box has been used to measure each cluster, the logarithmic slope of the ridge of those p.d.f.s can be interpreted as a crude fractal dimension of the attached vortices. Its numerical value of 2 suggests that the vortices are organized forming surfaces or shells. Such a behaviour is not strange in turbulent flows. For instance, Jiménez *et al.* (1993) observed that the worms of isotropic turbulence lie preferentially in the borders of large-scale velocity eddies.

The self-similarity of the tall attached clusters allows us to study their structure by looking at the p.d.f. of  $\mathbf{R} = \mathbf{r}/y_c$ , where  $\mathbf{r} = \mathbf{x} - \mathbf{x}_c$  is the position of a vortex point with respect to the centre of the bounding box,  $\mathbf{x}_c$ . The joint p.d.f. of  $r_x/y_c$  and  $r_y/y_c$  is shown in figure 11(b), revealing a clear pattern that does not depend on the Reynolds number for the present channels. Its local-average tilt angle has been computed from the locus of the streamwise location of the maximum of the p.d.f. at each  $r_y/y_c$ . At the bottom of the clusters it is about  $12^\circ$ , which agrees with the inclination of the streamwise vortices near the wall (Jeong *et al.* 1997), and increases to reach  $90^\circ$  at the

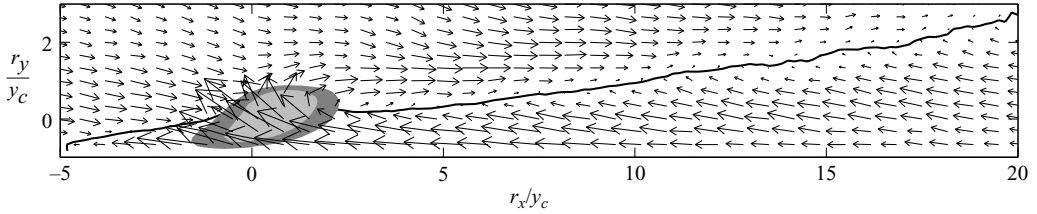


FIGURE 12. Quiver plot of the average perturbation velocity ( $\langle u' \rangle$ ,  $\langle v \rangle$ ) conditioned to the tall attached clusters, represented as a function of  $r_x/y_c$  and  $r_y/y_c$ . The plane shown is  $r_z=0$ . The shaded patches are the p.d.f. of the positions of the vortex cores and contain 50% and 75% of the data. The longest arrow is  $0.91u_\tau$ . The solid contour is  $\langle u' \rangle = 0$ . Case L950,  $\alpha \approx 2.5\alpha_c$ .

top of the clusters. The overall average inclination varies between  $42^\circ$  and  $46^\circ$  for the present flows, which is close to the  $45^\circ$  proposed by Theodorsen (1952) and reported by Head & Bandyopadhyay (1981). The most probable shape of the clusters agrees with that measured by Haidari & Smith (1994) on single vortex loops generated artificially in a laminar boundary layer, which is included in the figure, and also with that obtained by Zhou *et al.* (1999) in a laminar channel with a turbulent-like profile. Notice, however, that the p.d.f.s in figure 11(b) are widely scattered around the laminar hairpin, indicating that few if any of the individual clusters have that shape.

The average velocity field conditioned to the presence of a tall attached cluster is also consistent with a large-scale vortex loop, although the correspondence is hard to observe in individual eddies (Moin & Kim 1985; Robinson 1991*b*, see also §4.1). This is shown in figure 12, which displays a vector plot of the average velocity fluctuations in the  $(x, y)$ -plane bisecting the clusters. This conditional average is computed with respect to the centre of the cluster boxes, and is denoted  $\langle \cdot \rangle$ . For each cluster, the velocity fluctuations are expressed as functions of the scaled variable  $\mathbf{R}$ , and added to the average. For the streamwise component we have

$$\langle u' \rangle(\mathbf{R}) = \sum_{i=1}^{N_{TAC}} y_{c,i}^3 [u_i(\mathbf{R}y_{c,i} + \mathbf{x}_{c,i}) - U(r_y + y_{c,i})] / \sum_{i=1}^{N_{TAC}} y_{c,i}^3, \quad (4.4)$$

where  $N_{TAC}$  is the number of tall attached clusters,  $\mathbf{x}_{c,i}$  is the position of the  $i$ th object and  $u_i(\mathbf{x})$  is the streamwise velocity field associated with it. Notice that (4.4) weights the fluctuations with the volume of each cluster box and that the mean  $\langle u' \rangle$  for a given  $\mathbf{R}$  contains contributions from several wall distances.

The shaded patch in figure 12 is the p.d.f. of the positions of the vortex cores in the plane of the figure, similar to figure 11(b). A three-dimensional representation is figure 13. The data in figures 12 and 13 come from case L950 using  $\alpha \approx 2.5\alpha_c$ , but similar results are obtained at the remaining Reynolds numbers, and for the rest of the thresholds in figure 10. The conditional average in figure 12 shows a well-delimited region of  $\langle u' \rangle < 0$  and  $\langle v \rangle > 0$  close to the most probable positions of the vortices. This averaged ejection is flanked by two inclined counter-rotating vortices, which are the green objects around the meshed surface that represents the average location of the clusters in figure 13. They have been represented plotting an isosurface of the discriminant  $D_\diamond$ , computed from  $\langle u' \rangle$ . These results support the relation between the tall attached clusters and the organization of the velocity field in the logarithmic and outer regions, which was anticipated from figures 7(a) and 7(b).

#### 4.2.4. The clusters and their wakes

Figures 12 and 13 show a long region of  $\langle u' \rangle < 0$  extending downstream of the cluster, flanked by a pair of counter-rotating vortices. The structure spreads downstream from an origin near the cluster, suggesting that it has been created by the passage of the cluster itself. The idea that large-scale  $u$ -fluctuations can be modelled as the wakes of compact  $v$ -structures was already proposed by del Álamo *et al.* (2004) to explain the scaling of the  $u$ -spectrum in the logarithmic region, while Jiménez *et al.* (2004) showed that it explains many features of the streamwise velocity streaks of the buffer layer. The model also explains the qualitative features of figures 12 and 13. Assume that the cluster moves at a speed equal to the average of the mean velocity profile inside its vortex points. The flow closer to the wall is slower, and the wake appears towards the left-hand side. Above the ‘centre of gravity’ of the cluster, the mean flow is faster, and the wake moves towards the right-hand side (i.e. downstream). Note that the term ‘wake’ should be understood here in the sense of the structure created by a jet in a crossflow (Fric & Roshko 1994), which it resembles. The perturbation vorticity originates from the redistribution of the ambient shear, rather than from the interaction with the surface of a non-existent solid object.

Appealing as this model may be, we will now show that it can at most be used to explain the short upstream part of the  $u$ -structures in figures 12 and 13, because the clusters do not live long enough for their wakes to grow to the lengths observed downstream. Even so, for lack of a better notation and because of the slightly more complicated causal relationship discussed below, we will continue to refer to the perturbations in  $u$  associated with the clusters as their ‘wakes’.

The full analysis of the model would take us beyond the scope of the present paper, and it is left for other publications (del Álamo & Jiménez 2006; del Álamo *et al.* 2006). Here we estimate only the relevant orders of magnitude. The basic idea is that the clusters and their wakes are linear objects advected by the mean velocity profile and diffused by the eddy viscosity of the mean flow,  $\nu_T = \kappa u_\tau y$ . The results are variable-viscosity Orr–Sommerfeld and Squire equations for  $v$  and  $u$ , which in the former case reduce to a simple advection–diffusion equation for the streamwise vorticity  $\omega_x$  when the objects are very elongated streamwise. In that case, and assuming that the mean velocity profile is logarithmic, an initially compact  $v$ -structure grows linearly with time in all three directions, and moves downstream with a velocity that increases as it grows and samples higher points in the mean profile.

We have already associated the clusters with the wall-normal velocity, so that the self-similarity found above for the cluster dimensions is consistent with that result. The initial perturbation from which the cluster grows is not addressed by the model, except to assume that it is compact compared with later sizes. The  $v$  carried by the cluster serves as the initial source for the Squire equation for  $u$ , but the ‘wake’ keeps lengthening and diffusing even after the originating cluster has decayed. The lifetimes of the clusters can be estimated from the frequency–wavenumber spectrum  $\Phi_v$  of  $v$ , as the integral time scale defined by Wills (1964),

$$T_v(y) = \frac{\int \int \Phi_v(k_x, k_z, -k_x U_{adv}, y) dk_x dk_z}{\int \int \int \Phi_v(k_x, k_z, f, y) dk_x dk_z df}, \quad (4.5)$$

where  $f$  is the frequency and  $U_{adv}$  is the advection velocity of each wave component. They are given in figure 14(a) as functions of  $y$ . The integrals in (4.5) have been

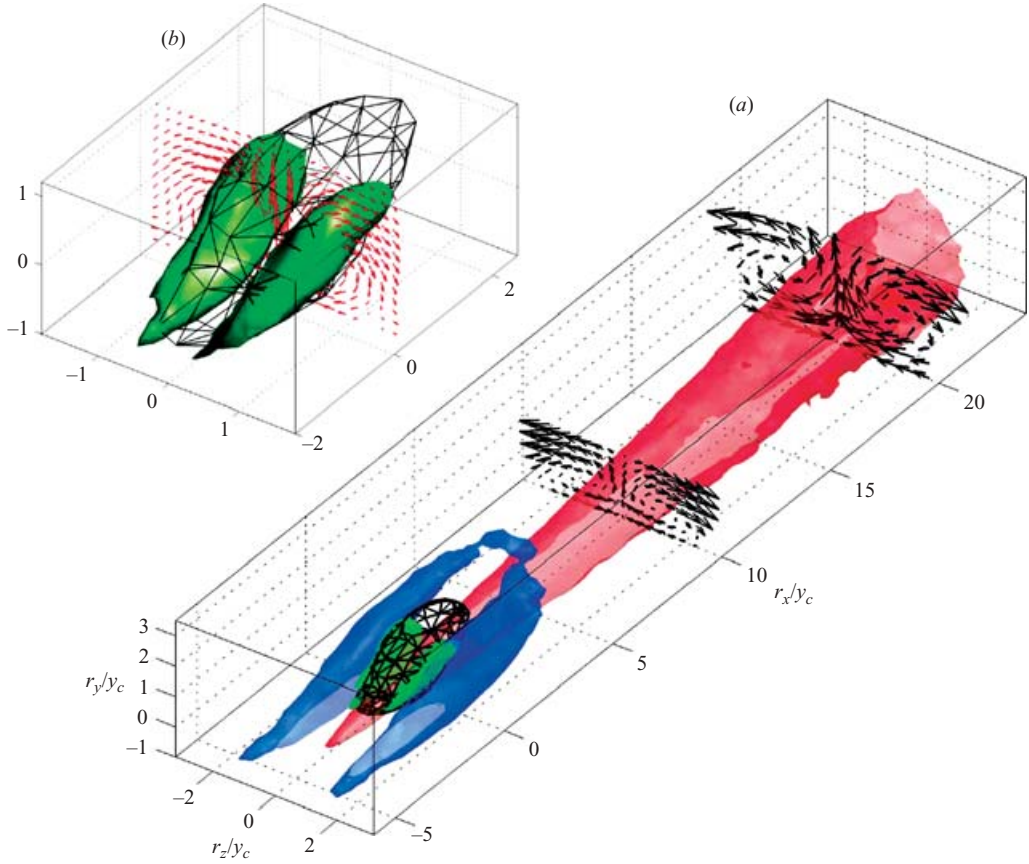


FIGURE 13. (a) Three-dimensional plot of the average velocity field conditioned to the tall attached clusters. The black mesh is an isosurface of the p.d.f. of the vortex positions and contains 57% of the data. The blue volume surrounding the cluster is the isosurface  $\langle u' \rangle^+ = 0.3$ . The red volume downstream of the cluster is the isosurface  $\langle u' \rangle^+ = -0.1$ . The green volumes are the isosurface  $D_{\delta}^+ = 10^{-3}$ . The vector plots represent  $(\langle v \rangle, \langle w \rangle)$  in the planes  $r_x/y_c = 10, 20$ . The scale of the arrows in the downstream plane has been magnified by a factor of 1.7 to facilitate their visualization. (b) A magnification of the surroundings of the average position of the clusters, including a vector plot of  $(\langle v \rangle, \langle w \rangle)$  in the plane  $x=0$ . The longest arrow measures  $0.5u_{\tau}$ . Case L950,  $\alpha \approx 2.5\alpha_c$ .

performed in the wavelength bands  $y/2 < \lambda_x < 2h$  and  $y/4 < \lambda_z < h$ . According to figures 7(a) and 7(b), these integration bands cover the sizes of the tall attached clusters that intercept each wall distance, which are those with  $\Delta_y > y$ . As in those figures, we have used the equivalence  $\Delta_y \approx y$  to convert wall distances into cluster heights.

The length of the wakes downstream of the clusters can be computed directly as the integral length of  $\langle u' \rangle$  along  $r_z = 0$  and  $\xi = y/r_x = \text{const}$ ,

$$l_x(\xi) = \frac{1}{\langle u' \rangle(0, 0, 0)} \int_0^L \langle u'(R_x, \xi R_x, 0) \rangle dR_x. \quad (4.6)$$

Figure 14(b) shows the average of  $l_x(\xi)$  for the range of slopes  $1/40 < \xi < 1/8$ , which is representative of the downstream wake in figure 12. The slope barely affects the

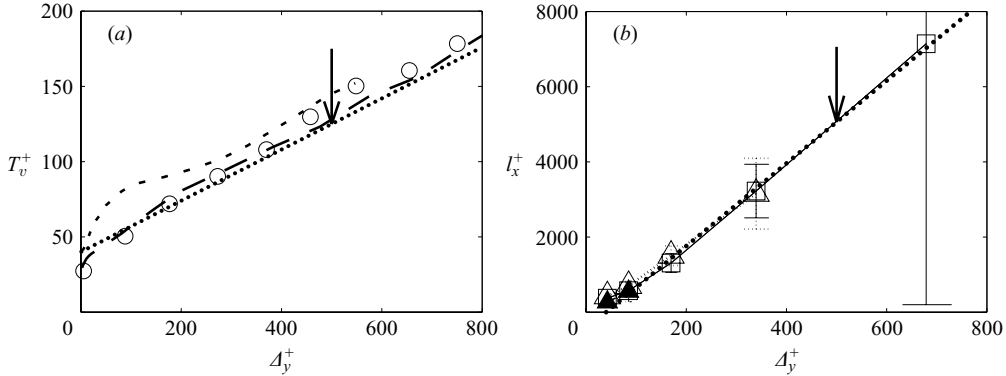


FIGURE 14. (a) Lifetimes  $T_v^+$  of the attached clusters, computed as the integral time of  $v$  in the wavelength bands  $y/2 < l_x < 2h$  and  $y/4 < l_x < h$ , and represented as functions of  $\Delta_y^+$ . Lines and symbols as in table 1. The thick dotted straight line is  $T_v^+ = 40 + 0.17\Delta_y^+$ . (b) Integral lengths  $l_x^+$  of the downstream wakes represented as functions of  $\Delta_y^+$ .  $\cdots \blacktriangle \cdots$ , case L180;  $\cdots \triangle \cdots$ , case L550;  $-\square-$ , case L950; the thick dotted straight line is  $l_x^+ = 11(\Delta_y^+ - 40)$ . The error bars represent the standard deviation of  $l_x$  induced by its dependence on the inclination of the rays on which it is computed. The vertical arrow represents the size,  $\Delta_y^+ = 500$ , of the typical tall attached cluster in the logarithmic region which is mentioned in the text. The threshold used in (3.1) is  $\alpha \approx 2.5\alpha_c$ .

integral lengths, as shown by the reasonably small error bars in the figure, which represent the r.m.s. of  $l_x$  obtained by assuming a uniform distribution of  $\xi$  in the above range. The only large error bar, at the last data point of the figure, is due to the small number of clusters extracted for the corresponding band of  $\Delta_y$ . The data in figure 14(b) come from the experiments L180, L550 and L950, but S950 and S1900 have been excluded because their small numerical boxes interfere with the longest wakes. The upper bound of integration in (4.6),  $L = 50$ , does not affect the integral length, as has been checked by comparing the results with those obtained for  $L = 30$  and 40.

Consider a typical tall attached cluster with  $\Delta_y^+ = 500$ . Figures 14(a) and 14(b) show that its lifetime is  $T_v^+ \approx 125$  and that the length of its downstream wake is  $l_x^+ \approx 5000$ . For this wake to develop from the difference  $\Delta U$  between the mean profile and the advection velocity of the cluster, we would require that  $\Delta U^+ \approx l_x^+/T_v^+ \approx 40$ . Similar velocity differences are required to explain the downstream wakes for the range of  $\Delta_y$  in figures 14(a) and 14(b). Even if these are only estimations, such high velocity differences are not available away from the wall. In the logarithmic region, for example,  $\Delta U^+ \approx U^+(y) - U^+(y_c) \approx \kappa^{-1} \log(y/y_c)$ , and  $\Delta U^+ = O(40)$  implies  $y/y_c = O(10^7)$ . Invoking self induction to slow the clusters with respect to the mean profile does not help. Even without considering the advection velocities of individual clusters, it is clear from figure 12 that any self-induced velocity would be  $O(u_\tau)$  at most.

Notice, on the other hand, that there are large velocity differences between the logarithmic layer and the wall region, which can result in longer upstream wakes. One of the results of the detailed analysis in del Álamo *et al.* (2006) is that the wakes grow to be much longer upstream of the cluster and near the wall than downstream and far from the wall. Those upstream wakes are compatible with the ‘tails’ found to the left of the cluster in figures 12 and 13.

This raises the question of what are the long downstream structures in the conditional statistics. The most plausible answer is that they are the upstream wakes of other larger clusters, aligned in the streamwise direction with those used for the conditioning, and that the latter are a consequence, rather than a cause of the downstream structure.

The clusters would then form groups of several members, with the larger individuals in front of the smaller ones. In this interpretation, the downstream wakes of figures 12 and 13 are long because they have been generated over long times upstream of taller clusters located even farther downstream. The averaged vortex pair in the far right of figure 13 would be a smeared version of the green vortices surrounding the conditioning cluster. Note that if every small cluster grew in this way to become large, the number of clusters of all dimensions should be roughly the same, contrary to the results in figure 10. This implies that most clusters disappear before they reach the upper logarithmic layer, either through decay or through merging with other clusters. Merging sets an upper limit to the number of surviving clusters, since it would occur as soon as the clusters begin to fill a volume fraction of order unity. This in turn implies that the percolation mechanism discussed in §3 is not just a representation artefact, but a physically relevant process.

Figure 14(a) shows that  $T_v$  increases linearly with  $\Delta_y$ , suggesting that the larger clusters are also older and that newborn individuals appear near the upstream edge of each cluster group. The inverse of the slope of  $T_v$  with respect to  $\Delta_y$  is the vertical velocity required to transport the clusters from the buffer layer into the outer region. The data indicate that sustained vertical growth velocities  $v^+ \approx 6$  would be required, which are too large for a quantity whose r.m.s. value is  $(\overline{v^2})^{1/2+} \approx 1$ . This suggests that at least some of the largest clusters are born away from the wall, either through a local instability or, as mentioned above, through the merging of smaller ones. The clusters grow self-similarly after that according to their sizes, not necessarily according to their ages, consistent with diffusion by an eddy viscosity that increases linearly with  $y$ . The linear relation between  $l_x$  and  $\Delta_y$  in figure 14(b) also suggests that the organization of the wakes associated to the cluster groups is self-similar.

Figure 15(a) displays contours of  $\langle u' \rangle / |\langle u' \rangle|(r_x, r_y, 0)|$ , taken at different wall distances and plotted as functions of  $r_x/y$  and  $r_z/y$ . This representation eliminates the effect of the variation with  $r_x$  of the wake intensity. For clarity, figure 15(a) shows a single isovalue, but similar results are obtained for any level corresponding with the interior of the low- $u$  wake. The collapse of the curves around a single parabola suggests that the overall shape of the wakes is a cone tangent to the wall, with its vertex slightly upstream of the conditioning cluster. This is reminiscent of Townsend's (1976, p. 157) conical eddy, and consistent with figure 13.

The angle  $\gamma$  formed by the intersection of the cone with the plane  $r_z = 0$  can be obtained from the position of the common vertex of the parabolas in figure 15(a),  $r_x/y \approx 7$ , and is roughly equal to  $8^\circ$ . When this angle is reduced to an intersection with the  $(x, z)$ -plane, it results in the parabola drawn as a dashed line in figure 15(a). The agreement between this parabola and the conditional data implies that the average conical eddies are roughly circular. Those angles agree with the inclination of the two-point correlation function of  $u$  reported by previous investigators. For example, Krogstad & Antonia (1994) found correlation angles of  $10^\circ$  in a turbulent boundary layer at  $Re_\theta = 6030$  and Liu, Adrian & Hanratty (2001) obtained  $6^\circ$ – $8^\circ$  in channels at  $Re_\tau = 315$ – $1414$ . Österlund (1999) measured inclinations that increase from  $7^\circ$  near the wall up to  $18^\circ$  in the outer layer of an  $Re_\theta = 9700$  boundary layer.

If we assume that all the clusters inside each wake follow the self-similar scalings (4.1), it is possible to estimate the average number of clusters that are present in each

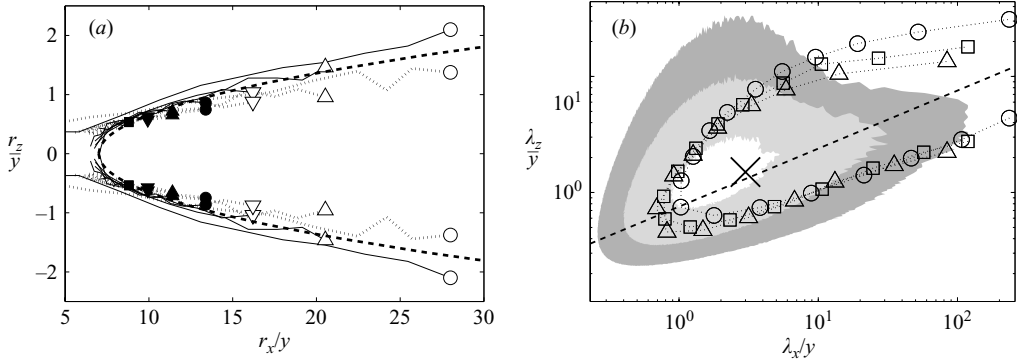


FIGURE 15. (a) Contours of the conditional streamwise perturbation velocity  $\langle u' \rangle$  in the wall-parallel plane. The data are normalized with the value of  $\langle u' \rangle$  at  $r_z = 0$ , and have been represented as functions of  $r_x/y$  and  $r_z/y$ . The value represented is  $\langle u' \rangle / |\langle u'(r_x, y, 0) \rangle| = -0.33$ .  $\cdots$ ,  $Re_\tau = 550$ ;  $\text{---}$ ,  $Re_\tau = 950$ . The curves come from different values of  $y$  as indicated by the markers.  $\circ$ ,  $y = 0.92y_c$ ;  $\triangle$ ,  $y = 1.3y_c$ ;  $\nabla$ ,  $y = 1.6y_c$ ;  $\bullet$ ,  $y = 1.9y_c$ ;  $\blacktriangle$ ,  $y = 2.3y_c$ ;  $\blacktriangledown$ ,  $y = 2.6y_c$ ;  $\blacksquare$ ,  $y = 2.9y_c$ . The dashed curve is the parabola  $r_z^2 = (r_x/7 - y)y$ . The threshold used in (3.1) is  $\alpha \approx 2.5\alpha_c$ . (b) Two-dimensional spectral densities  $\phi^{2D}$  as functions of the wavelengths  $\lambda_x/y$  and  $\lambda_z/y$ . The line contours are  $\phi_u^{2D+} = 0.1$  and each of them comes from a different wall distance.  $\circ$ ,  $y^+ = 100$ ;  $\square$ ,  $y^+ = 200$ ;  $\triangle$ ,  $y^+ = 300$ . The shaded contours are  $\phi_v^{2D+} = 0.01(\times 3)0.1$ , at  $y^+ = 200$ . Case L950.  $\text{---}$ ,  $\lambda_z = 2(\lambda_x y/7)^{1/2}$ . The  $\times$  marks the sizes of the tall attached clusters in (4.1), using the equivalence  $\Delta = \lambda$  and  $y_c = y/2$ .

wake from the inclination angle  $\gamma$ . Consider for simplicity a cluster centred at unit wall distance and a second one that is  $p$  times larger, centred at a wall distance  $p$ . According to (4.1), the streamwise separation between the two objects should be at least  $3 + 3p$  for them to be detected as different, and hence the wall-normal distance between their centres should satisfy

$$p - 1 \geq (3 + 3p) \tan \gamma. \quad (4.7)$$

The minimum solution to this inequality for the value of  $\gamma$  given above,  $p = 2.5$ , is the ratio of the sizes of adjacent clusters when they are packed most tightly inside the cone. It fixes the maximum number of clusters per wake,  $N_{max}$ . Assuming that the smallest cluster has  $\Delta_y^+ = 100$  and the largest one has  $\Delta_y^+ = 2Re_\tau$ , we obtain  $N_{max} = \log(Re_\tau/50)/\log(p)$ , which varies from 1.4 to 4.0 for  $180 < Re_\tau < 1900$ . This number increases very weakly with the Reynolds number, reaching  $N_{max} = 10$  only when  $Re_\tau > 5 \times 10^5$ .

The intersection of the conical  $u'$  structures with  $(x, y)$ -planes is also reminiscent of the low- $u$  ramps observed in two-dimensional sections of laboratory boundary layers by Adrian *et al.* (2000), and in channels by Christensen & Adrian (2001). Those authors reported that the ramps are associated with trains of spanwise sections of vortices. Adrian *et al.* (2000) proposed that those trains are the heads of self-propelled hairpin vortices flanking the ramps, whose joint combined induction against the mean stream generates the low- $u$  regions. Our results are much less organized, and suggest an alternative picture, in which the tall attached clusters are distributed along the ramps with increasing streamwise separations rather than flanking them continuously. The clusters are associated to compact wall-normal motions that generate  $u$  fluctuations by stirring the mean shear, and the fluctuations spread owing to the action of incoherent background turbulence instead of by the coherent induction of the cluster vortices.

Other more mechanistic explanations are possible; for example, Hutchins, Ganapathisubramani & Marusic (2004) documented the meandering of instantaneous  $u$ -structures, and Tomkins & Adrian (2003) showed that individual buffer-layer streaks merge with each other. There is no doubt that all these effects are present, as well as possibly many others, but we believe that the simplest way to summarize all the random events that influence the spreading of a particular structure is diffusion by the background turbulent fluctuations, which can be modelled approximately by the variable eddy viscosity mentioned above. Del Álamo *et al.* (2004) have shown that such an approximation could describe the scaling of the two-dimensional spectrum of the streamwise velocity.

If we define the wake of a cluster as extending from  $0 < r_x/\Delta_y < 12$ ,  $-1 < r_z/\Delta_y < 1$  and  $0 < y/\Delta_y < 2$ , based on the integral lengths and aspect ratios given above, the wakes of the maximal set of tall attached clusters defined by  $\alpha \approx \alpha_c$  fill the channel almost completely. When the intersections between wakes are counted, they cover from 9.8 to 19.8 times the volume of the channel, meaning that each point belongs on average to several wakes, and that smaller wakes live within larger ones. It also suggests that the dynamics of the wakes are roughly linear, because they can be superimposed without affecting each other substantially. The observations by Meinhart & Adrian (1995) and by Adrian *et al.* (2000) of nested uniform- $u$  ramps in instantaneous  $(x, y)$ -planes of boundary layers agree with these results.

The large volume fractions occupied by the wakes imply that these structures have to contribute substantially to the Reynolds stresses, and that they should affect the scaling of the energy spectrum across the channel. In the wall-parallel plane, the square-root spreading of the average velocity field conditioned to the tall attached clusters agrees with that of the two-dimensional energy spectral density,  $\phi^{2D}$ . This is observed in figure 15(b), which displays  $\phi_u^{2D}$  and  $\phi_v^{2D}$  in the logarithmic region of case L950. The location of the maximum of  $\phi_v^{2D}$  in figure 15(b) coincides roughly with the cross that marks the mean size of the clusters, but there are important contributions to the energy spectral densities at larger scales, consistent with the long wakes in figures 12 and 13. Those contributions are organized along the dashed straight line that represents the square-root spreading of the conditional averages in figure 15(a). This agrees with the results in figure 15(a) for the spreading of the conditional structures, but it extends them to the much longer lengths available from the spectra.

The conical shape of the downstream mean velocity field implies that the mechanism of cluster formation has to be self-similar and relatively well organized, with clusters of height  $\Delta_y$  forming in parts of the wakes which have transverse dimensions of the same order. Otherwise the downstream mean flow field, which is conditioned on the existence of a cluster at  $r_x=0$  and which is scaled with the height of that cluster, would quickly lose coherence.

The general picture that develops is one of compact  $v$ -structures, tagged here by the presence of vorticity clusters, with lives which are proportional to their sizes, created by some instability process in the upstream wakes left by still larger clusters in front of them. The clusters thus created grow themselves and leave new wakes that give rise to new clusters behind them. This mechanism is reminiscent of the vortex-streak regeneration cycle of the buffer layer, although it now involves the more complex structures in the logarithmic region. This continuous creation of new clusters at all heights, not necessarily at the wall, is consistent with the observation that, even if the intensity of the clusters must decay as they grow in size, the observed r.m.s. intensities of the clusters are independent of their sizes.



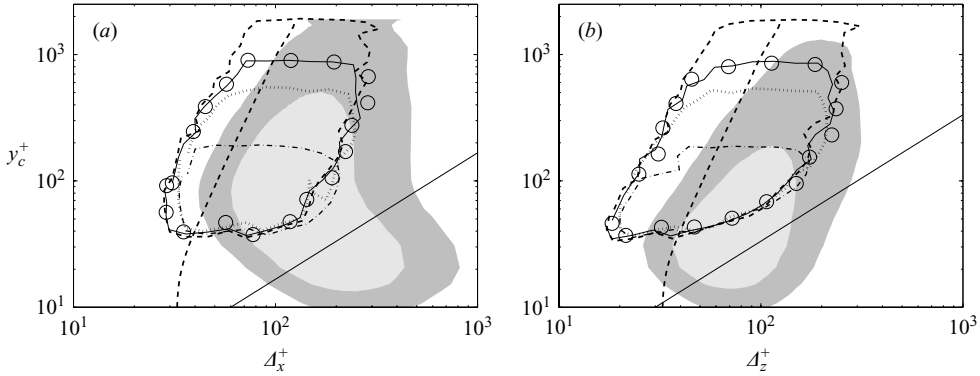


FIGURE 16. Probability density functions of the logarithms of the size  $\Delta$  of the detached clusters, and of the wall distances  $y_c$  of their centres. Lines and symbols as in table 1,  $\alpha \approx 2.5\alpha_c$ . The iso-probability contours contain 75% of the data; the shaded contours are  $\phi_\omega$  and represent 1/3 and 2/3 of its maximum value; we have used the correspondence  $\lambda \approx \Delta$  and  $y_c \approx y$ ; (a)  $p(\log(\Delta_x), \log(y_c))$  and  $\phi_\omega(\lambda_x, y)$ ; (b)  $p(\log(\Delta_z), \log(y_c))$  and  $\phi_\omega(\lambda_z, y)$ . The dashed curves on the ridges of the p.d.f.s are  $\Delta = 20\eta$ , and the solid ones are  $\Delta_x = 6y_c$  and  $\Delta_z = 3y_c$ .

There is, moreover, no shortage of candidate wake instabilities to act as possible generators for the clusters. The most obvious one is a Kelvin–Helmholtz instability of the fairly sharp velocity gradient bounding the wake from above, although much more work is required to either confirm or negate this possibility.

#### 4.3. Detached clusters

The scaling of the detached clusters in the present channels differs significantly from that of the tall attached ones. This can be observed in figures 16(a) and 16(b), which display the p.d.f.s of their sizes in the wall-parallel plane and of the wall distance of their centres, similar to figures 7(a) and 7(b). The p.d.f.s peak approximately along the dashed line that corresponds to  $\Delta = 20\eta(y_c)$ , indicating that the sizes of the detached clusters are proportional to the Kolmogorov scale. Similar results are obtained for the p.d.f.s of  $\Delta_y$  and  $y_c$ , not shown.

The detached clusters are much smaller than the tall attached ones, which are represented by the solid straight lines in figures 16(a) and 16(b). They are also smaller than  $y_c$ , which suggests that the equivalence  $y = y_c$  is approximately correct for them. That equivalence, together with  $\lambda = \Delta$ , has been used in figures 16(a) and 16(b) to compare the p.d.f.s with the spectral enstrophy densities,  $\phi_\omega(\lambda, y)$ , from case S1900. Both magnitudes agree reasonably well, suggesting that the enstrophy, and hence the energy dissipation, is organized in the form of detached vortex clusters above the near-wall region. This result supports the ideas of Perry & Chong (1982), who noted that wall attached eddies alone could not explain the inertial and dissipation ranges of the spectrum. The factor of 20 that multiplies  $\eta$  in the data of figures 16(a) and 16(b) is consistent with Frisch (1995), who noted that, in experimental isotropic turbulence, viscosity becomes important for scales smaller than  $30\eta$ .

The detached vortices are distributed preferably inside the low- $u$  wakes, as can be deduced from the relative location of the  $\langle u' \rangle$  contours and the p.d.f.s of the vortex positions in figures 17(a) and 17(b). These figures are analogous to figure 12, and display the average velocity field conditioned to the detached clusters in the plane  $r_z = 0$ . The statistics in figure 17(a) are dominated by the large number of detached clusters that are found far from the wall (see figure 5), and the clusters appear

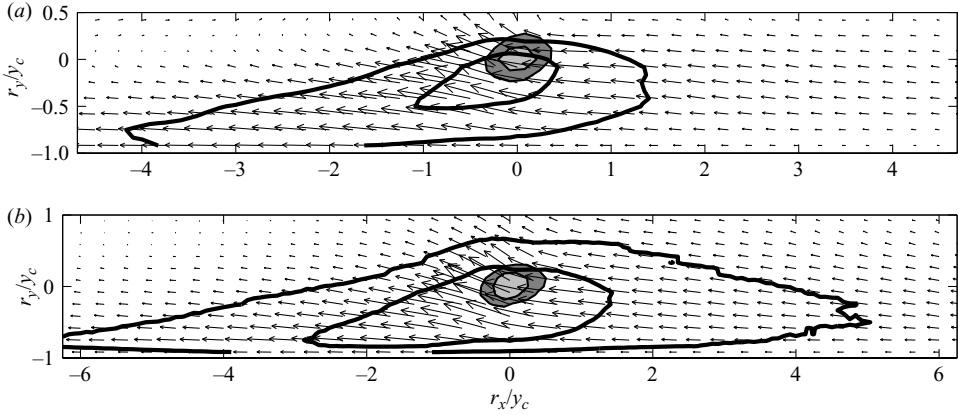


FIGURE 17. Quiver plots of the average perturbation velocity conditioned to the presence of each detached cluster, represented as functions of  $r_x/y_c$  and  $r_y/y_c$ . The plane shown is  $r_z = 0$ . The shaded patches are the p.d.f.s of the position of the vortex cores and contain 50% and 75% of the data. The arrows in the two plots have the same scale as those in figure 12 and the longest one (in *b*) is  $1.1u_\tau$ . The thick solid contours are  $\langle u' \rangle^+ = -0.4, -0.2$ . Case L950,  $\alpha \approx 2.5\alpha_c$ . All the clusters are considered in (a), but only those with  $y_{min}^+ < 150$  are considered in (b).

at the top-downstream end of the wakes. However, when we consider only those clusters below  $y^+ = 150$ , as in figure 17(b), their location inside the wake is more centred. These results agree with Tanahashi *et al.* (2003, 2004), who reported that the maximum of the conditional p.d.f. of  $u'$  for  $Q > 0$  is negative in channels up to  $Re_\tau = 800$ . Figure 13 suggests an explanation for this behaviour. The interior of the wake is formed by fluid that has been pumped up from the vicinity of the wall, which carries vortices that were formed close to the wall, where the turbulence is stronger. This is consistent with Kang, Tanahashi & Miyauchi (2004), who showed that in the channels of Tanahashi *et al.* (2003, 2004), the vortices that reside in low- $u$  structures are stronger than those in high- $u$  ones.

## 5. Conclusions

We have analysed the vortex clusters found in numerical turbulent channels at friction Reynolds numbers  $180 < Re_\tau < 1900$ . The clusters are defined as groups of adjacent points where the discriminant of the velocity gradient tensor is larger than a certain fraction of its r.m.s. value in the wall-parallel plane, and we have introduced a way to define this fraction in terms of the percolation properties of the vortices. We have shown that the use of this non-uniform threshold offers one solution to the identification problems related to the inhomogeneity of the flow, and that the local properties of the extracted vortices are similar to those of the intense worms of isotropic turbulence (Jiménez & Wray 1998).

We have seen that the logarithmic region is populated by two classes of clusters. One of them consists of small vortex packets that are detached from the wall and which are roughly homogeneous and isotropic. The other one is formed by tall clusters rooted in the near-wall region below  $y^+ \approx 20$ .

The tall attached clusters are linked to velocity structures which are more intense than their background, which is probably why their constituent vortices percolate

locally and reach the near-wall region. On average, the velocity eddies associated with these objects consist of a wall-normal ejection surrounded by two inclined counter-rotating vortices. Although this average structure is consistent with a single large-scale vortex loop, most of the individual clusters are more complex. This is especially true for the larger ones, which have relatively high internal Reynolds numbers.

When each tall attached cluster is inscribed into a parallelepipedal box aligned to the Cartesian grid, the boxes are self-similar, with dimensions  $\Delta_x \approx 3\Delta_y$  and  $\Delta_z \approx 1.5\Delta_y$ . These are also the dimensions of the structures with signatures of hairpin packets extracted in laboratory experiments at comparable Reynolds numbers (Nakagawa & Nezu 1981; Ganapathisubramani *et al.* 2003; Tomkins & Adrian 2003).

We have probed the influence of the tall attached clusters on the outer region by analysing their density per unit height and per unit wall-parallel area,  $n_s(\Delta_y)$ . We have seen that this influence is independent of  $Re_\tau$  if  $n_s$  goes approximately as  $\Delta_y^{-3}$ , and that it decreases with the Reynolds number if  $n_s$  decays faster. In our channels, the decay exponent of  $n_s$  increases with decreasing identification threshold  $\alpha$ , and reaches  $-3$  when  $\alpha$  is lowered sufficiently. The corresponding cluster set contains an important fraction of the transverse Reynolds stresses at all wall distances. If  $\alpha$  is lowered further, the decay exponent does not increase any more owing to the percolation of the whole vortex population. Interestingly, Townsend (1976, p. 154) already assumed implicitly that  $n_s \sim \Delta_y^{-3}$  in his attached-eddy model, but, to our knowledge, that decay exponent had not been documented before.

The conditionally averaged flow downstream of the tall attached clusters shows large structures of low  $u$  that can be modelled as wakes spreading self-similarly under an eddy viscosity  $\nu_T \approx \kappa u_\tau y$ . These wakes spread linearly in their  $(x, y)$ -bisecting plane, similar to the ramps reported by Adrian *et al.* (2000) and Christensen & Adrian (2001), and as  $x^{1/2}$  in wall-parallel planes, in agreement with the scaling of the two-dimensional energy spectrum in the logarithmic region (del Álamo *et al.* 2004). We have shown that this behaviour is consistent with a cone tangent to the wall along the  $x$ -axis, similar to Townsend's (1976, p. 157) conical eddy. The wakes cover the whole volume of our experiments, and hence contribute substantially to the streamwise Reynolds stresses.

We have estimated the lifetimes of the tall attached clusters by measuring the decay in the frequency-wavenumber spectrum of the wall-normal velocity. The length of the associated wakes has been measured from the integral length of the conditionally averaged streamwise velocity field. The results indicate first that the clusters are too short-lived to have grown from the wall to their observed heights, and second that the conditional wakes downstream of the clusters are too long to have been created by the conditioning cluster. From them we conclude that the conditioning cluster can only be a consequence of the presence of the downstream wake, while the shorter upstream wake may have formed from the cluster.

Owing to the observed self-similarity, the downstream wake must actually correspond to the structure upstream of other, larger clusters in front of the conditioning one. The signatures of these forward clusters appear as a pair of weak counter-rotating vortices in the conditional field. Assuming that the clusters in a given wake follow the self-similar size relation given above, we have shown that the number of clusters per wake grows logarithmically with the  $Re_\tau$  and remains relatively small.

This leads to a description in which clusters are repeatedly started by wakes left by still larger clusters in front of them. We have noted that the mechanism may be as simple as a Kelvin–Helmholtz instability of the shear layer surrounding the wake.

This picture is similar to the turbulence regeneration cycle of the buffer layer, but it is less organized because it involves flow structures that are turbulent themselves, such as the clusters and the wakes.

From a kinematic point of view, it is practically impossible to distinguish between the models based on hairpin packets of Head & Bandyopadhyay (1981) and of Adrian *et al.* (2000), and the wake model presented here. The discussion essentially boils down to whether the vorticity is considered to be the derivative of the velocity, or whether the velocity is seen as the integral of vorticity. However, the wake model provides a simple dynamical mechanism by which the diffusion of perturbations to the mean shear by the background turbulence generates self-similar conical velocity structures. We personally find it difficult to explain how the dynamics of systems of discrete vortices may lead to self-similarity.

The cluster-wake pairs need not be exclusive to turbulent flows over smooth walls. Flores & Jiménez (2004) showed that the energy spectra in the outer region of turbulent channels with modified boundary conditions that inhibit the formation of a buffer layer are also consistent with the existence of these structures. The only macroscopic feature that those flows share with smooth-walled ones is the existence of a mean shear, which suggests that the clusters and the wakes are direct consequences of it. Although it cannot be ruled out that some near-wall ejections may occasionally be started by top-down interactions of the kind postulated by Hunt & Morrison (2000), both the concentration of clusters near the walls and the location of the large velocity scales in the lee of the clusters suggest that this mechanism is not the primary one controlling near-wall dynamics.

The overall picture presented in this paper describes the structures that take part in the self-similar range of the turbulent logarithmic region. To our knowledge, this is the first time that the organization of a turbulent self-similar range has been characterized at this level, not only for the case of wall flows, but also for turbulent flows in general.

This work was supported in part by the Spanish CICYT contract BFM2003-03434. The Spanish Ministry of Education partially supported J. C. A. with a FPU graduate fellowship and R. D. M. with a Sabbatical visit. In the USA, this work was supported by the AFOSR under grant F49620-01-1-0181, the NSF under grant CTS-001435, and by the CSAR, which is funded by the DOE through University of California grant B341494. We are especially indebted to the CEPBA/IBM centre of the U. Politècnica de Catalunya, which graciously donated the computer time needed for some of the simulations, to the San Diego Supercomputer Center and to the US Department of Defense Major Shared Resource Centers, who provided computer time for the remaining ones. It is a pleasure to acknowledge fruitful discussions with O. Flores. We also thank M. Tanahashi for providing in digital format the data on vortex properties used in figure 4(a), and P. Chakraborty for supplying a preprint of his paper.

#### REFERENCES

- ACARLAR, M. S. & SMITH, C. R. 1987 A study of hairpin vortices in a laminar boundary layer. Part 1. Hairpin vortices generated by a hemisphere protuberance. *J. Fluid Mech.* **175**, 1–41.
- ADRIAN, R. J., MEINHART, C. D. & TOMKINS, C. D. 2000 Vortex organization in the outer region of the turbulent boundary layer. *J. Fluid Mech.* **422**, 1–53.

- DEL ÁLAMO, J. C. & JIMÉNEZ, J. 2003 Spectra of the very large anisotropic scales in turbulent channels. *Phys. Fluids* **15**, L41–L44.
- DEL ÁLAMO, J. C. & JIMÉNEZ, J. 2006 Linear energy amplification in turbulent channels. *J. Fluid Mech.* **559**, 205–213.
- DEL ÁLAMO, J. C., JIMÉNEZ, J., ZANDONADE, P. & MOSER, R. D. 2004 Scaling of the energy spectra of turbulent channels. *J. Fluid Mech.* **500**, 135–144.
- DEL ÁLAMO, J. C., FLORES, O., JIMÉNEZ, J., ZANDONADE, P. & MOSER, R. D. 2006 The linear dynamics of the turbulent logarithmic region. In preparation.
- BLACKBURN, H. M., MANSOUR, N. N. & CANTWELL, B. J. 1996 Topology of fine-scale motions in turbulent channel flow. *J. Fluid Mech.* **310**, 269–292.
- CHAKRABORTY, P., BALACHANDAR, S. & ADRIAN, R. J. 2005 Relationships between local vortex identification schemes. *J. Fluid Mech.* **535**, 189–214.
- CHONG, M. S., PERRY, A. E. & CANTWELL, B. J. 1990 A general classification of three-dimensional flow fields. *Phys. Fluids A* **2**, 765–777.
- CHONG, M. S., SORIA, J., PERRY, A. E., CHACIN, J., CANTWELL, B. J. & NA, Y. 1998 Turbulence structures of wall-bounded flows using DNS data. *J. Fluid Mech.* **357**, 225–247.
- CHRISTENSEN, K. T. & ADRIAN, R. J. 2001 Statistical evidence of hairpin vortex packets in wall turbulence. *J. Fluid Mech.* **431**, 433–443.
- CUCITORE, R., QUADRIO, M. & BARON, A. 1999 On the effectiveness and limitations of local criteria for the identification of a vortex. *Eur. J. Mech. B/Fluids* **18**, 261–282.
- FLORES, O. & JIMÉNEZ, J. 2004 Effect of wall-boundary disturbances on turbulent channel flows. In *Advances in Turbulence X* (ed. H. I. Anderson & P.-A. Krogstad), pp. 235–238. CIMNE, Barcelona.
- FRIC, T. F. & ROSHKO, A. 1994 Vortical structure in the wake of a transverse jet. *J. Fluid Mech.* **279**, 1–47.
- FRISCH, U. 1995 *Turbulence*, p. 203. Cambridge University Press.
- GANAPATHISUBRAMANI, B., LONGMIRE, E. K. & MARUSIC, I. 2003 Characteristics of vortex packets in turbulent boundary layers. *J. Fluid Mech.* **478**, 35–46.
- HAIDARI, A. H. & SMITH, C. R. 1994 The generation and regeneration of single hairpin vortices. *J. Fluid Mech.* **277**, 135–162.
- HEAD, M. R. & BANDYOPADHYAY, P. 1981 New aspects of turbulent boundary-layer structure. *J. Fluid Mech.* **107**, 297–338.
- HITES, M. 1997 Scaling of high-Reynolds number turbulent boundary layers in the national diagnostic facility. PhD thesis, Illinois Inst. of Technology.
- HUNT, J. C. R. & MORRISON, J. F. 2000 Eddy structure in turbulent boundary layers. *Eur. J. Mech. B/Fluids* **19**, 673–694.
- HUNT, J. C. R., WRAY, A. A. & MOIN, P. 1988 Eddies, streams, and convergence zones in turbulent flows. In *Proc. Summer Program*, pp. 9–14. Center for Turbulence Research, Stanford University.
- HUTCHINS, N., GANAPATHISUBRAMANI, B. & MARUSIC, I. 2004 Dominant spanwise Fourier modes, and the existence of very large coherence in turbulent boundary layers. In *15th Australasian Fluid Mechanics Conference* (ed. M. Behnia, W. Lin & G. D. McBain). AMC00127.
- JEONG, J., HUSSAIN, F., SCHOPPA, W. & KIM, J. 1997 Coherent structures near the wall in turbulent channel flow. *J. Fluid Mech.* **332**, 185–214.
- JIMÉNEZ, J. & WRAY, A. A. 1998 On the characteristics of vortex filaments in isotropic turbulence. *J. Fluid Mech.* **373**, 255–285.
- JIMÉNEZ, J., WRAY, A. A., SAFFMAN, P. G. & ROGALLO, R. 1993 The structure of intense vorticity in isotropic turbulence. *J. Fluid Mech.* **255**, 65–90.
- JIMÉNEZ, J., FLORES, O. & GARCÍA-VILLALBA, M. 2001 The large-scale organization of autonomous turbulent wall regions. In *Annu. Res. Briefs*, pp. 317–327. Center for Turbulence Research, Stanford University.
- JIMÉNEZ, J., DEL ÁLAMO, J. C. & FLORES, O. 2004 The large-scale dynamics of near-wall turbulence. *J. Fluid Mech.* **505**, 179–199.
- KANG, S.-J., TANAHASHI, M. & MIYAUCHI, T. 2004 Coherent fine-scale eddies and large-scale structures in wall turbulence. In *Advances in Turbulence X* (ed. H. I. Anderson & P.-A. Krogstad), pp. 603–606. CIMNE, Barcelona.

- KIDA, S., GOTO, S. & MAKIHARA, T. 2002 Low-pressure vortex analysis in turbulence: life, structure, and dynamical role of vortices. In *Tubes, Sheets and Singularities in Fluid Dynamics* (ed. K. Bajer & H. K. Moffat), pp. 181–190. Kluwer.
- KIM, J., MOIN, P. & MOSER, R. D. 1987 Turbulence statistics in fully developed channel flow at low Reynolds number. *J. Fluid Mech.* **177**, 133–166.
- KROGSTAD, P.-A. & ANTONIA, R. A. 1994 Structure of turbulent boundary layers on smooth and rough walls. *J. Fluid Mech.* **277**, 1–21.
- LIU, Z., ADRIAN, R. J. & HANRATTY, T. J. 2001 Large-scale modes of turbulent channel flow: transport and structure. *J. Fluid Mech.* **448**, 53–80.
- MARUSIC, I. 2001 On the role of large-scale structures in wall turbulence. *Phys. Fluids* **13**, 735–743.
- MEINHART, C. D. & ADRIAN, R. J. 1995 On the existence of uniform momentum zones in a turbulent boundary layer. *Phys. Fluids* **7**, 694–696.
- MOIN, P. & KIM, J. 1985 The structure of the vorticity field in turbulent channel flow. Part 1. Analysis of instantaneous fields and statistical correlations. *J. Fluid Mech.* **155**, 441–464.
- MOISY, F. & JIMÉNEZ, J. 2004 Geometry and clustering of intense structures in isotropic turbulence. *J. Fluid Mech.* **513**, 111–122.
- MOSER, R. D., KIM, J. & MANSOUR, N. N. 1999 Direct numerical simulation of turbulent channel flow up to  $Re_\tau = 590$ . *Phys. Fluids* **11**, 943–945.
- NAGAOSA, R. & HANDLER, R. A. 2003 Statistical analysis of coherent vortices near a free surface in a fully developed turbulence. *Phys. Fluids* **15**, 375–394.
- NAKAGAWA, H. & NEZU, I. 1977 Prediction of the contributions to the reynolds stress from bursting events in open channel flow. *J. Fluid Mech.* **80**, 99–128.
- NAKAGAWA, H. & NEZU, I. 1981 Structure of space–time correlations of bursting phenomena in an open channel flow. *J. Fluid Mech.* **104**, 1–43.
- ÖSTERLUND, J. 1999 Experimental studies of zero pressure-gradient turbulent boundary layer flow. PhD thesis, Kungl Tekniska Högskolan.
- PERRY, A. E. & CHONG, M. S. 1982 On the mechanism of wall turbulence. *J. Fluid Mech.* **119**, 173–217.
- PERRY, A. E. & MARUSIC, I. 1995 A wall-wake model for the turbulence structure of boundary layers. 1. Extension of the attached eddy hypothesis. *J. Fluid Mech.* **298**, 361–388.
- PERRY, A. E., HENBEST, S. & CHONG, M. S. 1986 A theoretical and experimental study of wall turbulence. *J. Fluid Mech.* **119**, 163–199.
- ROBINSON, S. K. 1991a Coherent motions in the turbulent boundary layer. *Annu. Rev. Fluid Mech.* **23**, 601–639.
- ROBINSON, S. K. 1991b The kinematics of turbulent boundary layer structure. PhD thesis, NASA Ames Research Center.
- STAUFFER, D. 1985 *Introduction to Percolation Theory*. Taylor & Francis.
- TANAHASHI, M., MIYAUCHI, T. & IKEDA, J. 1997 Identification of coherent fine-scale structure in turbulence. In *Simulation and Identification of Coherent Structure in Flow* (ed. J. N. Sørensen, E. J. Hopfinger & N. Aubry), pp. 131–140. Kluwer.
- TANAHASHI, M., KANG, S.-J., MIYAMOTO, T., SHIOKAWA, S. & MIYAUCHI, T. 2003 Scaling of fine scale eddies in turbulent channel flows up to  $Re_\tau = 800$ . In *Proc. of the 3rd Intl Symp. Turbulence and Shear Flow Phenomena*, pp. 9–14. Begell House.
- TANAHASHI, M., KANG, S.-J., MIYAMOTO, T., SHIOKAWA, S. & MIYAUCHI, T. 2004 Scaling of fine scale eddies in turbulent channel flows up to  $Re_\tau = 800$ . *Intl J. Heat Mass Transfer* **25**, 331–340.
- THEODORSEN, T. 1952 Mechanism of turbulence. In *Proc. Second Midwestern Conf. on Fluid Mechanics, Ohio, Ohio State University*, pp. 1–18.
- TOMKINS, C. D. & ADRIAN, R. J. 2003 Spanwise structure and scale growth in turbulent boundary layers. *J. Fluid Mech.* **490**, 37–74.
- TOWNSEND, A. A. 1976 *The Structure of Turbulent Shear Flows*, 2nd edn. Cambridge University Press.
- WILLS, J. 1964 On convection velocities in turbulent shear flows. *J. Fluid Mech.* **20**, 417–432.
- ZAGAROLA, M. V. & SMITS, A. J. 1998 Mean-flow scaling of turbulent pipe flow. *J. Fluid Mech.* **373**, 33–79.
- ZHOU, J., ADRIAN, R. J., BALACHANDAR, S. & KENDALL, T. M. 1999 Mechanisms for generating coherent packets of hairpin vortices in channel flow. *J. Fluid Mech.* **387**, 353–396.